

# Looking for imprints of the first stellar generations in metal-poor bulge field stars <sup>★</sup>

C. Siqueira-Mello<sup>1</sup>, C Chiappini<sup>2</sup>, B. Barbuy<sup>1</sup>, K. Freeman<sup>3</sup>, M. Ness<sup>4</sup>, E. Depagne<sup>5</sup>, E. Cantelli<sup>1</sup>, M. Pignatari<sup>6,7,8</sup>, R. Hirschi<sup>9,10</sup>, U. Frischknecht<sup>9,11</sup>, G. Meynet<sup>12</sup>, and A. Maeder<sup>12</sup>

<sup>1</sup> Universidade de São Paulo, IAG, Rua do Matão 1226, Cidade Universitária, São Paulo 05508-900, Brazil; e-mail: cesar.mello@usp.br

<sup>2</sup> Leibniz-Institut für Astrophysik Potsdam (AIP), An der Sternwarte 16, 14482, Potsdam, Germany; e-mail: cristina.chiappini@aip.de

<sup>3</sup> Mount Stromlo Observatory, Research School of Astronomy & Astrophysics, Australian National University College of Physical and Mathematical Sciences, Cotter Road, Weston Creek, ACT 2611, Australia

<sup>4</sup> Max Planck Institute for Astronomy, Königstuhl 17, 69117 Heidelberg, Germany

<sup>5</sup> South African Astronomical Observatory (SAAO), P.O. Box 9, Observatory 7935, South Africa

<sup>6</sup> E.A. Milne Centre for Astrophysics, Dept of Physics & Mathematics, University of Hull, HU6 7RX, United Kingdom

<sup>7</sup> Konkoly Observatory, Research Centre for Astronomy and Earth Sciences, Hungarian Academy of Sciences, Konkoly Thege Miklos ut 15-17, H-1121 Budapest, Hungary

<sup>8</sup> NuGrid collaboration, <http://www.nugridstars.org>

<sup>9</sup> Astrophysics group, Lennard-Jones Laboratories, Keele University, ST5 5BG, Staffordshire, UK

<sup>10</sup> Kavli Institute for the Physics and Mathematics of the Universe (WPI), University of Tokyo, 5-1-5 Kashiwanoha, Kashiwa, 277-8583, Japan

<sup>11</sup> Dept. of Physics, University of Basel, Klingelbergstr. 82, 4056, Basel, Switzerland

<sup>12</sup> Observatoire de Genève, Chemin des Maillettes 51, Sauverny, CH-1290 Versoix, Switzerland

Received; accepted

## ABSTRACT

**Context.** Efforts to look for signatures of the first stars have concentrated on metal-poor halo objects. However, the low end of the bulge metallicity distribution has been shown to host some of the oldest objects in the Milky Way and hence this Galactic component potentially offers interesting targets to look at imprints of the first stellar generations. As a pilot project, we selected bulge field stars already identified in the ARGOS survey as having  $[\text{Fe}/\text{H}] \approx -1$  and oversolar  $[\alpha/\text{Fe}]$  ratios, and we used FLAMES-UVES to obtain detailed abundances of key elements that are believed to reveal imprints of the first stellar generations.

**Aims.** The main purpose of this study is to analyse selected ARGOS stars using new high-resolution ( $R \sim 45,000$ ) and high-signal-to-noise ( $S/N > 100$ ) spectra. We aim to derive their stellar parameters and elemental ratios, in particular the abundances of C, N, the  $\alpha$ -elements O, Mg, Si, Ca, and Ti, the odd-Z elements Na and Al, the neutron-capture s-process dominated elements Y, Zr, La, and Ba, and the r-element Eu.

**Methods.** High-resolution spectra of five field giant stars were obtained at the 8m VLT UT2-Kueyen telescope with the UVES spectrograph in FLAMES-UVES configuration. Spectroscopic parameters were derived based on the excitation and ionization equilibrium of Fe I and Fe II. The abundance analysis was performed with a MARCS LTE spherical model atmosphere grid and the Turbospectrum spectrum synthesis code.

**Results.** We confirm that the analysed stars are moderately metal-poor ( $-1.04 \leq [\text{Fe}/\text{H}] \leq -0.43$ ), non-carbon-enhanced (non-CEMP) with  $[\text{C}/\text{Fe}] \leq +0.2$ , and  $\alpha$ -enhanced. We find that our three most metal-poor stars are nitrogen enhanced. The  $\alpha$ -enhancement suggests that these stars were formed from a gas enriched by core-collapse supernovae, and that the values are in agreement with results in the literature for bulge stars in the same metallicity range. No abundance anomalies (Na – O, Al – O, Al – Mg anti-correlations) were detected in our sample. The heavy elements Y, Zr, Ba, La, and Eu also exhibit oversolar abundances. Three out of the five stars analysed here show slightly enhanced  $[\text{Y}/\text{Ba}]$  ratios similar to those found in two other metal-poor bulge GCs (NGC 6522 and M 62).

**Conclusions.** This sample shows enhancement in the first-to-second peak abundance ratios of heavy elements, as well as dominantly s-process element excesses. This can be explained by different nucleosynthesis scenarios: a) the main r-process plus extra mechanisms, such as the weak r-process; b) mass transfer from Asymptotic Giant Branch (AGB) stars in binary systems; c) an early generation of fast-rotating massive stars. Larger samples of moderately metal-poor bulge stars, with detailed chemical abundances, are needed to better constrain the source of dominantly s-process elements in the early Universe.

**Key words.** Galaxy: Bulge - Stars: Abundances, Atmospheres

## 1. Introduction

Efforts to find the chemical imprints in the oldest stars of the Milky Way left by the first stellar generations (hereafter, first stars) have focused on very metal-poor halo stars with  $[\text{Fe}/\text{H}] \sim -3$ . Some cosmological simulations have suggested that at least

Send offprint requests to: C. Siqueira Mello Jr. ([cesar.mello@usp.br](mailto:cesar.mello@usp.br)).

<sup>★</sup> Observations collected at the European Southern Observatory, Paranal, Chile (ESO), under programmes 089.B-0208(A).

half of the first stars should have formed in the Galactic bulge (e.g. Tumlinson 2010). Consequently, this Galactic component is a potential source of interesting targets to be explored. These simulations suggest that the oldest stars, which have formed at the highest density peaks (bulge), have enriched the surrounding interstellar medium (ISM) on very short timescales. Chemical evolution models also suggest that the old bulge formed on short timescales (e.g. Grieco et al. 2012).

Barbuy et al. (2009, 2014) searched for evidence of the signatures of formation of the first stellar generations in the old bulge globular cluster NGC 6522, potentially the oldest Milky Way globular cluster. The results were discussed in the framework of the early fast-rotating massive stars, coined Spinstars, or mass transfer from AGB stars (Chiappini et al. 2011; Ness et al. 2014).

The central parts of the Galaxy, where the oldest stars most probably preferentially reside, have not been targeted extensively, partly due to the very small fraction of metal-poor stars in the predominantly metal-rich bulge region. The situation started to change with the Bulge Radial Velocity Assay (BRAVA; Kunder et al. 2012) and the Abundances and Radial velocity Galactic Origins Survey (ARGOS; Freeman et al. 2013), and the new data being obtained by the Apache Point Observatory Galactic Evolution Experiment (APOGEE; Majewski et al. 2015) in the near infrared. In particular, the Galactic bulge ARGOS Survey, an AAOmega/AAT spectroscopic survey that measured radial velocities, metallicities and  $[\alpha/\text{Fe}]$  ratio of about 28, 000 stars (Freeman et al. 2013), opened the opportunity to explore the bulge field metal-poor stars. The rather large number of targets observed by ARGOS provided the opportunity of identifying bulge stars with metallicities  $[\text{Fe}/\text{H}] \approx -1$ , and estimating oversolar  $[\alpha/\text{Fe}]$  ratios.

Using ARGOS targets, we began a pilot project aimed at obtaining detailed chemical abundances of metal-poor bulge field stars to look for possible chemical imprints of the first stars. One of these imprints could be an overabundance of dominantly s-process elements (e.g. Meynet et al. 2006; Pignatari et al. 2008; Chiappini et al. 2011; Frischknecht et al. 2012, 2015; Barbuy et al. 2014; Cecutti et al. 2013; Cescutti & Chiappini 2014). Indeed, enhancements of Sr, Y, and Zr relative to Ba and La, and an excess of Ba or La relative to Eu, in very old stars of the Milky Way can be attributed to the s-process activation in early generations of fast rotating massive stars, which pollute the primordial material prior to the formation of the oldest bulge (halo) field stars. An alternative possibility is an s-process contribution from massive AGB stars bound in a binary system (e.g. Bisterzo et al. 2010). Otherwise the idea that has been more widely accepted is that these elements were produced by the r-process in early times (Truran 1981). An extra process is also claimed to produce the enhancement of the lightest heavy elements relative to the heaviest elements, in literature called the lighter element primary process (LEPP; Travaglio et al. 2004; Bisterzo et al. 2014) or weak r-process (Wanajo & Ishimaru 2006). The astrophysical scenarios with neutrino-driven winds are considered the most promising sites (Wanajo 2013; Arcones & Thielemann 2013; Fujibayashi et al. 2015; Niu et al. 2015).

The aim of this work is to obtain detailed chemical constraints from field bulge stars. Here, we analyse five of these stars at high spectral resolution, using UVES spectra. We derive element abundances of C, N, the  $\alpha$ -elements O, Mg, Si, Ca, and Ti, the odd-Z elements Na and Al, the dominantly s-elements Y, Zr, Ba, and La, and the r-element Eu. The observations are described in Sect. 2. Photometric effective temperatures are derived in Sect. 3. Spectroscopic parameters are derived in Section

**Table 1.** Log of the spectroscopic observations: date, time, exposure time, seeing, and air mass at the beginning and at the end of the observation.

Run	Date	Time	Exp.	Seeing	Airmass
			(s)	(")	
1	2012-07-12	04:07:43.1	2775	0.8–0.8	1.0–1.1
2	2012-08-02	02:59:47.1	2775	0.3–0.7	1.0–1.1
3	2012-07-21	03:59:12.6	2775	1.0–1.3	1.0–1.1
4	2012-07-23	02:46:14.3	2775	0.7–1.0	1.0–1.0
5	2012-08-02	03:57:27.9	2775	1.0–1.5	1.1–1.2
6	2012-08-03	23:31:53.7	2775	0.8–0.8	1.2–1.1
7	2012-08-22	01:22:09.9	2775	0.7–0.8	1.0–1.1
8	2012-08-21	23:56:35.2	2308	0.9–0.9	1.0–1.0
9	2012-08-22	02:24:20.8	2775	0.7–0.7	1.1–1.2
10	2012-08-23	01:48:05.3	2775	1.0–1.1	1.0–1.1

4 and abundance ratios are computed in Sect. 5. A discussion is presented in Sect. 6 and conclusions are drawn in Sect. 7.

**Table 2.** Geocentric radial velocity in each of the ten exposure runs with corresponding heliocentric radial velocities and mean heliocentric radial velocity, in  $\text{km s}^{-1}$ .

run	RV <sub>G</sub>	RV <sub>B</sub>	RV <sub>G</sub>	RV <sub>B</sub>
	221		224	
run1	-96.9±2.1	-106.7±2.1	-105.9±2.1	-115.6±2.1
run2	-88.3±1.6	-107.1±1.6	-96.7±2.0	-115.4±2.0
run3	-92.4±1.8	-106.3±1.8	-101.1±2.0	-115.0±2.0
run4	-66.9±2.1	-81.5±2.1	-101.6±3.8	-116.2±3.8
run5	-87.5±2.4	-106.3±2.4	-96.3±2.3	-115.1±2.3
run6	-87.8±1.4	-106.9±1.4	-96.2±1.8	-115.3±1.8
run7	-81.9±2.0	-107.1±2.0	-90.4±2.1	-115.5±2.1
run8	-81.7±3.4	-106.7±3.4	-89.3±3.0	-114.3±3.0
run9	-80.8±1.6	-106.1±1.6	-89.3±1.6	-114.5±1.6
run10	-81.9±1.4	-107.4±1.4	-90.2±1.5	-115.7±1.5
Mean		-106.7±2.1		-115.3±2.4
	230		235	
run1	-71.1±2.1	-80.9±2.1	145.4±1.4	135.6±1.4
run2	-62.2±2.1	-80.9±2.1	154.3±1.6	135.6±1.6
run3	-66.2±1.9	-80.1±1.9	150.6±1.6	136.7±1.6
run4	—	—	149.7±1.5	135.1±1.5
run5	—	—	155.5±1.6	136.6±1.6
run6	-61.5±2.5	-80.6±2.5	155.0±1.5	135.9±1.5
run7	-55.9±1.9	-81.0±1.9	160.9±1.6	135.7±1.6
run8	-54.7±4.4	-79.7±4.4	162.0±1.6	137.0±1.6
run9	-54.7±1.9	-80.0±1.9	162.2±1.6	136.9±1.6
run10	-55.5±1.8	-80.9±1.8	161.0±1.4	135.6±1.4
Mean		-80.5±2.3		136.1±1.6
	238			
run1	-137.1±1.5	-146.9±1.5		
run2	-128.0±1.6	-146.7±1.6		
run3	-132.3±1.5	-146.3±1.5		
run4	-132.6±1.8	-147.3±1.8		
run5	-127.4±1.6	-146.3±1.6		
run6	-127.5±1.7	-146.6±1.7		
run7	-121.5±1.5	-146.7±1.5		
run8	-121.0±1.9	-146.0±1.9		
run9	-120.8±1.4	-146.1±1.4		
run10	-121.5±1.4	-147.0±1.4		
Mean		-146.6±1.7		

**Table 3.** Identifications, coordinates, magnitudes, and reddening.  $JHK_s$  from both 2MASS and VVV surveys are given.

star	2MASS ID	$\alpha$ (J2000)	$\delta$ (J2000)	l(°)	b(°)	V	J	H	$K_s$	$J_{VVV}$	$H_{VVV}$	$K_{sVVV}$	$E(B - V)^a$	$E(B - V)^b$	S/N
221	18033285-3117421	18:03:32.80	-31:17:42.04	359.92	-4.54	17.9	13.95	13.08	12.84	13.85	13.08	12.84	0.73	0.85	101
224	18034522-3117379	18:03:45.18	-31:17:37.72	359.94	-4.57	17.9	13.96	13.10	12.84	13.77	13.02	12.79	0.77	0.90	79
230	18033933-3114044	18:03:39.28	-31:14:04.24	359.98	-4.53	18.6	14.70	13.94	13.56	14.62	13.85	13.61	0.76	0.89	65
235	18032741-3109441	18:03:27.40	-31:09:43.96	0.02	-4.45	16.2	12.63	11.81	11.60	12.58	11.71	11.57	0.72	0.83	175
238	18031238-3106210	18:03:12.35	-31:06:20.92	0.05	-4.38	17.0	13.14	12.24	12.02	13.03	12.25	11.95	0.71	0.82	152

**References.** <sup>a</sup>Schlafly & Finkbeiner (2011), <sup>b</sup>Schlegel et al. (1998)

**Table 4.** Photometric temperatures derived using the calibrations by Alonso et al. (1999) for several colours and the final temperature adopted. Colours from 2MASS and VVV catalogues were used, with reddening  $E(B - V)$  based on Schlegel et al. (1998) (first line) and Schlafly & Finkbeiner (2011) (second line) for each star.

Star	$T_{\text{eff}}(V - K)$	$T_{\text{eff}}(V - K)$	$T_{\text{eff}}(J - H)$	$T_{\text{eff}}(J - H)$	$T_{\text{eff}}(J - K)$	$T_{\text{eff}}(J - K)$	Average $T_{\text{eff}}$ (K)
	2MASS	VVV	2MASS	VVV	2MASS	VVV	
221	4179.3	4172.5	4281.9	4304.9	4404.8	4478.9	4303.7
	4401.3	4392.8	4400.9	4425.4	4576.7	4658.7	4476.0
224	4249.3	4211.3	4348.7	4415.8	4436.3	4644.4	4384.3
	4502.9	4455.1	4479.0	4550.9	4621.7	4853.9	4577.3
230	4244.7	4267.8	4666.3	4348.2	4379.3	4526.9	4405.5
	4493.2	4522.1	4817.5	4476.7	4555.6	4719.7	4597.5
235	4476.1	4443.6	4437.9	3997.6	4640.7	4445.2	4406.9
	4764.5	4723.9	4564.5	4096.8	4834.1	4617.7	4600.3
238	4182.7	4135.7	4180.5	4258.3	4336.5	4261.4	4225.9
	4396.8	4338.9	4289.0	4371.5	4495.3	4412.7	4384.0

## 2. Observations and reductions

We used the UVES spectrograph (Dekker et al. 2000), in FLAMES-UVES mode, for the observation of five metal-poor ( $[\text{Fe}/\text{H}] \sim -1$ ) bulge stars, at a high resolution of  $R = 45,000$  with a slit width of  $0.8''$ . Centring the wavelength at  $5800 \text{ \AA}$ , the spectral wavelength range  $4800 - 6800 \text{ \AA}$  with a gap at  $5708 - 5825 \text{ \AA}$  was obtained. The red chip ( $5800 - 6800 \text{ \AA}$ ) has ESO CCD#20, an MIT backside illuminated, with  $4096 \times 2048$  pixels, and pixel size  $15 \times 15 \mu\text{m}$ . The blue chip ( $4800 - 5800 \text{ \AA}$ ) uses ESO Marlene EEV CCD#44, backside illuminated, with  $4102 \times 2048$  pixels, and pixel size  $15 \times 15 \mu\text{m}$ . The pixel scale is  $0.0147 \text{ \AA}/\text{pix}$ , with  $\sim 7.5$  pixels per resolution element at  $6000 \text{ \AA}$ .

The log of observations is given in Table 1. The data were reduced using the UVES pipeline, within ESO/Reflex software (Ballester et al. 2000; Modigliani et al. 2004). The spectra were flatfielded, optimally-extracted and wavelength calibrated with the FLAMES-UVES pipeline. The spectra were normalized, corrected for radial-velocity shift, and combined to produce the final average data. Figure 1 illustrates the quality of the spectra for the five sample stars.

### 2.1. Radial velocities

In Table 2, we report the geocentric and heliocentric radial velocities measured with IRAF/FXCOR for each of the 10 runs, together with their mean values. A solar spectrum was adopted as the template. We used a solar synthetic spectrum to confirm the correction for the radial-velocity shift. We note that the heliocentric radial velocity for the star 221 obtained in run 4 is excessively different in comparison to others, so it was excluded from the final average spectrum. In addition, the IRAF routine

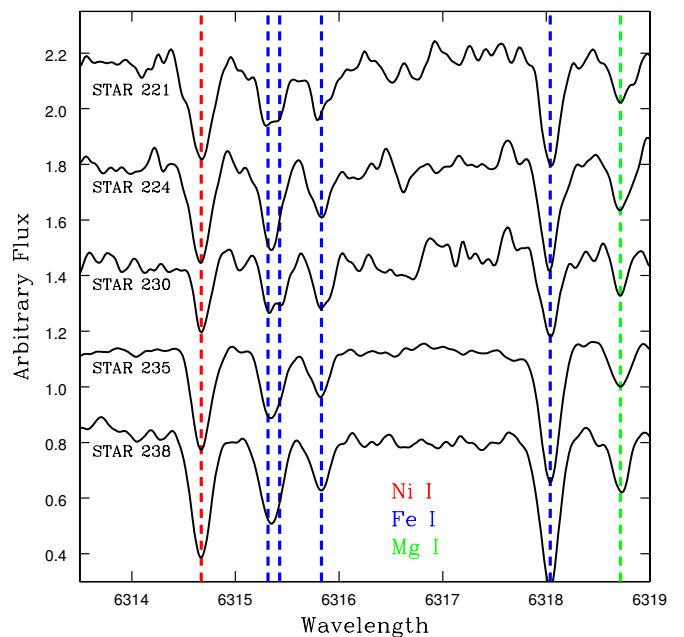


**Fig. 1.** Portion of the final data. The dashed lines show Ni I (red), Fe I (blue), and Mg I (green) lines located in this wavelength range.

was not able to measure the radial velocities for the star 230 using two runs (4 and 5), and they were also discarded.

### 3. Photometric stellar parameters

#### 3.1. Temperatures

The selected stars, their OGLE and 2MASS designations, coordinates, magnitudes, and S/N values corresponding to an average of clean windows in the range 6400–6500 Å, are given in Table 3.  $V$  magnitudes computed using individual reddening from Schlegel et al. (1998) in the direction of each star are adopted from the ARGOS survey (Freeman et al. 2013),  $JHK_s$  magnitudes from 2MASS (Skrutskie et al. 2006), and VVV surveys (Saito et al. 2012). In this section we derive the photometric temperatures, to compare with results from the ARGOS survey, as explained below.

We calculated photometric temperatures based on three colours:  $(V - K)$ ,  $(J - H)$ , and  $(J - K)$ . Calibrations by Alonso et al. (1999) were applied, with reddening  $E(B - V)$  computed with the Galactic reddening and extinction calculator from the Infrared Processing and Analysis Center (IRSA)<sup>1</sup>. Results based on Schlegel et al. (1998) and on Schlafly & Finkbeiner (2011) were used. The extinction laws given by Rieke & Lebofsky (1985) were adopted. Colours from 2MASS were transformed into the ESO photometric system and from this into the TCS (Telescopio Carlos Sánchez) system, following the relations established by Carpenter (2001) and Alonso et al. (1998). The VVV  $JHK_s$  colours were transformed to the 2MASS  $JHK_s$  system, using relations by Soto et al. (2013).

The derived photometric effective temperatures are listed in Table 4. In our sample, the values obtained using the reddening from Schlafly & Finkbeiner (2011) are  $\Delta T_{\text{eff}} = 182 \pm 13$  K higher than the results with reddening from Schlegel et al. (1998). The more affected temperature is the one obtained with the colour  $(V - K)$ , for which the average difference is  $\Delta T_{\text{eff}} = 243 \pm 22$  K. The differences between temperatures derived with the VVV and 2MASS  $JHK_s$  colours are  $\Delta T_{\text{eff}} = 12 \pm 45$  K, which indicates that there is no significant trend in the temperature owing to the survey chosen for our sample. The outlier is the star 235: the temperatures obtained with 2MASS  $JHK_s$  colours are  $\Delta T_{\text{eff}} = 232 \pm 9$  K higher than the results from the VVV survey.

Table 5 shows the parameters obtained from the ARGOS survey to our set of stars. As described in Freeman et al. (2013), the effective temperatures were derived from the  $(J - K)$  colours using the calibration from Bessell et al. (1998) with interstellar reddening from Schlegel et al. (1998). The values for  $\log g$ ,  $[\text{Fe}/\text{H}]$ , and  $[\alpha/\text{Fe}]$  were determined by comparing the observed spectra with a grid of synthetic spectra computed in LTE with the code MOOG 2010 (Snedden 1973) and using 1D model atmospheres, described in Castelli & Kurucz (2004). A constant microturbulence velocity  $\xi = 2.0$  km s<sup>-1</sup> was adopted in their method.

The photometric temperatures derived in this work are systematically lower than the results from ARGOS:  $\Delta T_{\text{eff}} = 388 \pm 54$  K if the reddening from Schlegel et al. (1998) is adopted and  $\Delta T_{\text{eff}} = 206 \pm 59$  K for the reddening maps of Schlafly & Finkbeiner (2011). These differences are smaller when our temperatures derived with the  $(J - K)$  colours are compared:  $\Delta T_{\text{eff}} = 278 \pm 58$  K and  $\Delta T_{\text{eff}} = 98 \pm 66$  K, respectively. Indeed, Freeman et al. (2013) report a mean temperature lower by 100 K when the empirical calibration from Alonso et al. (1999) is applied, and this difference is higher (up to 200 K) for the most metal-poor stars in the sample.

**Table 5.** Galactocentric velocities, atmospheric parameters, and enhancement in  $\alpha$ -elements for the present sample from the Galactic bulge ARGOS Survey.

Star	$V_{\text{gal}}$ (km s <sup>-1</sup> )	$T_{\text{eff}}$ (K)	$\log g$ [cgs]	$[\text{Fe}/\text{H}]$	$[\alpha/\text{Fe}]$
221	-96.06	4669.54	1.6	-0.80	0.40
224	-105.17	4757.18	1.8	-0.82	0.35
230	-71.73	4697.27	1.4	-0.84	0.03
235	146.01	4929.72	2.4	-0.80	0.52
238	-136.31	4613.03	2.4	-0.80	0.33

### 4. Spectroscopic stellar parameters

#### 4.1. Equivalent widths

To derive the atmospheric parameters, we measured the equivalent widths (EW) of selected iron lines, using the IRAF software. We decided to retain the lines with  $10 < \text{EW} < 100$  mÅ located in the range 6100 – 6800 Å to derive the atmospheric parameters, which is the spectral region with the highest S/N ratio available. The EW values measured manually were adopted since this method allows a better continuum placement and an individual evaluation of each line.

Table A.1 presents the complete list of lines, describing the atomic data, the EW measured with IRAF, and the individual iron abundance derived using the atmospheric parameters adopted.

#### 4.2. Atmospheric parameters

The photometric temperatures, together with the gravity and metallicity values from the ARGOS survey as given in Table 5, are adopted as a first guess to calculate the excitation and ionization equilibria of Fe I and Fe II lines. The MARCS spherical model atmosphere grids (Gustafsson et al. 2008) with  $1 M_{\odot}$  and the code Turbospectrum (Alvarez & Plez 1998) in the equivalent width mode were used, with solar abundances adopted from Asplund et al. (2009). Applying an automatic routine on a grid of models with  $\Delta T_{\text{eff}} = 20$  K,  $\Delta \log g = 0.1$  [cgs], and  $\Delta \xi = 0.1$  km s<sup>-1</sup>, the final surface gravity  $\log g$  was chosen to minimize  $[\text{Fe II}/\text{H}] - [\text{Fe I}/\text{H}]$ , the final microturbulence velocity  $\xi$  was chosen to minimize the dependence of  $[\text{Fe I}/\text{H}]$  on  $\log(\text{EW}/\lambda)$ , and the final temperature was obtained by the excitation equilibrium. The grid was recomputed successively with a new metallicity in each step, and the range used for each parameter was selected to avoid local solutions.

Figure 2 shows the excitation and ionization equilibria for two different typical cases: the star 221, which presents a spectrum with a low S/N; and the star 235, which presents a high-quality spectrum. Lines with abundances out of the region limited by  $\pm 3\sigma$ , where  $\sigma$  is the standard error of the mean, were removed from the computations of final metallicities.

The black dots are the abundances obtained from Fe I lines, and the red squares are the results from the Fe II lines. The blue dashed lines represent the linear fit to data, and the blue dotted lines are the same function moved vertically by .

The derived stellar parameters are reported in Table 6, as well as the number of Fe I and Fe II lines retained, the difference  $\Delta_{\text{II-I}} = [\text{Fe II}/\text{H}] - [\text{Fe I}/\text{H}]$  obtained with the final models, and the parameters from the linear fit to data in each case. The angular coefficients and the values of  $\Delta_{\text{II-I}}$  are null within the error bar, which indicate that there are no relevant trends in the excita-

<sup>1</sup> <http://irsa.ipac.caltech.edu/applications/DUST/>

**Table 6.** Spectroscopic parameters adopted for each star. We also present the number of iron lines used for each star to derive the atmospheric parameters. The difference  $\Delta_{II-I} = [\text{Fe II}/\text{H}] - [\text{Fe I}/\text{H}]$  shows the quality in the ionization equilibrium, and the parameters from the linear fitting  $[\text{Fe I}/\text{H}] = a_{EW} * \log(EW/\lambda) + b_{EW}$  for microturbulence and  $[\text{Fe I}/\text{H}] = a_{exc} * exc.pot + b_{exc}$  for effective temperature.

Star	$T_{\text{eff}}$ (K)	$\log g$ [cgs]	[Fe I/H]	[Fe II/H]	[Fe/H] <sub>model</sub>	$\xi$ (km s <sup>-1</sup> )	#Fe I	#Fe II	$\Delta_{II-I}$	$a_{EW}$	$b_{EW}$	$a_{exc}$	$b_{exc}$
221	4620	2.0	-0.88±0.24	-0.91±0.17	-0.90	1.0	31	2	-0.035	+0.00±0.12	+6.63±0.55	+0.004±0.045	+6.61±0.15
224	5000	3.5	-0.62±0.36	-0.60±0.30	-0.65	0.8	61	4	+0.015	+0.02±0.10	+6.96±0.48	+0.013±0.044	+6.84±0.15
230	4960	3.0	-1.04±0.40	-1.03±0.18	-1.10	0.8	58	5	+0.0038	+0.02±0.11	+6.57±0.52	+0.087±0.056	+6.17±0.19
235	4680	2.2	-0.94±0.15	-0.95±0.09	-0.95	1.1	45	7	-0.012	+0.00±0.03	+6.59±0.17	-0.002±0.024	+6.57±0.08
238	4720	2.9	-0.43±0.18	-0.42±0.07	-0.50	1.0	33	5	-0.0077	+0.00±0.07	+7.07±0.35	+0.027±0.031	+6.98±0.11

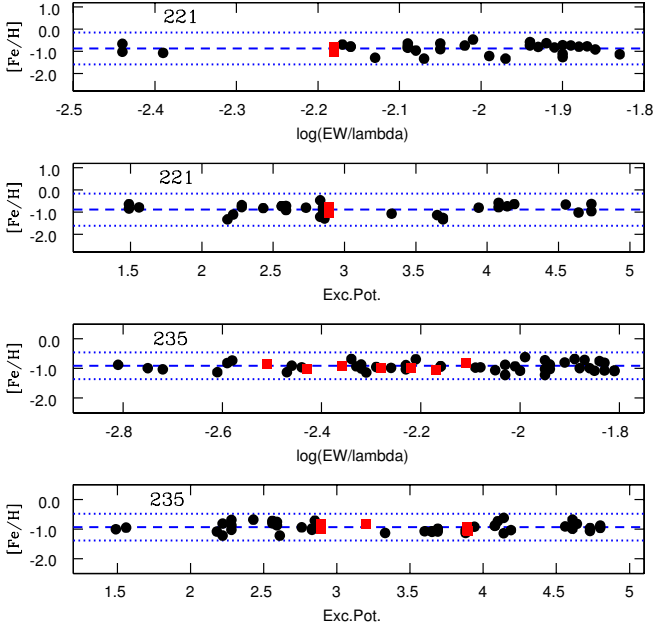


**Fig. 2.** Ionization and excitation equilibria of Fe lines for the stars 221 and 235, using the newly derived atmospheric parameters. The black dots are the abundances obtained from the Fe I lines, the red squares are those from the Fe II lines, the blue dashed lines represent the linear fit to data, and the dotted blue lines are the same linear fit moved vertically by  $\pm 3\sigma$ , where  $\sigma$  is the standard error of the mean.

tion and ionization equilibria. The parameters can be compared with the results derived from the mid-resolution survey ARGOS, reported in Table 5.

## 5. Abundance ratios

A line-by-line fitting was carried out to derive the abundances, using the spectrum synthesis code Turbospectrum (Alvarez & Plez 1998), which includes scattering in the blue and UV domain, molecular dissociative equilibrium, and collisional broadening by H, He, and H<sub>2</sub>, following Anstee & O’Mara (1995), Barklem & O’Mara (1997), and Barklem et al. (1998). The atomic line lists were adopted from the Vienna Atomic Line Database compilation (VALD3; Piskunov et al. 1995), together with the Turbospectrum molecular line lists (B. Plez, private communication). For lines used to derive abundances, as reported in Table A.2, the oscillator strengths were adopted from Barbay et al. (2014), except when described. Hyperfine structures were adopted for the lines relevantly affected by this effect. Tables 7 and 9 show the adopted final abundances.

**Table 8.** Adopted Arcturus abundances.

El.	$A(X)_{\text{Arcturus}}$	El.	$A(X)_{\text{Arcturus}}$
C	8.32 <sup>[1]</sup>	Ca	5.94 <sup>[1]</sup>
N	7.68 <sup>[2]</sup>	Sc	2.81 <sup>[1]</sup>
O	8.66 <sup>[2]</sup>	Ti	4.66 <sup>[1]</sup>
Na	5.82 <sup>[1]</sup>	V	3.58 <sup>[1]</sup>
Mg	7.47 <sup>[1]</sup>	Cr	4.99 <sup>[1]</sup>
Al	6.26 <sup>[1]</sup>	Mn	4.74 <sup>[1]</sup>
Si	7.30 <sup>[1]</sup>	Co	4.71 <sup>[1]</sup>
K	4.99 <sup>[1]</sup>	Ni	5.73 <sup>[2]</sup>

**References.** [1]: Ramírez & Allende Prieto (2011); [2]: Meléndez et al. (2003).

### 5.1. Carbon and nitrogen

To evaluate the adopted line list in the regions selected for carbon and nitrogen abundances, we used the Arcturus spectrum (Hinkle et al. 2000) as a reference star. Our benchmark analysis is based on the stellar parameters described in Meléndez et al. (2003):  $T_{\text{eff}} = 4275$  K,  $\log g = 1.55$  [cgs],  $[\text{Fe}/\text{H}] = -0.54$ , and  $\xi = 1.65$  km s<sup>-1</sup>. We adopted chemical abundances from Ramírez & Allende Prieto (2011) and Meléndez et al. (2003), as presented in Table 8.

To measure the carbon abundances we used the C<sub>2</sub>(0,1) molecular bandhead. The region is extended and a mean abundance was derived from the overall fit, however the bandhead at 5635.3 Å received more weight in the fitting procedure. The line list for <sup>12</sup>C<sub>2</sub>, <sup>13</sup>C<sub>2</sub>, and <sup>12</sup>C<sup>13</sup>C was adopted from Wahlin & Plez (2005), which contains transitions from the Swan (d<sup>3</sup>Π - a<sup>3</sup>Π) electronic band. The solar isotopic fraction for <sup>12</sup>C (98.9%) and <sup>13</sup>C (1.1%) was adopted (Asplund et al. 2009). Figure 3 shows in the upper panel the synthetic spectrum computed for Arcturus (blue solid line), which is in very good agreement with observations. For the sample stars, the C<sub>2</sub>(0,1) molecular bandhead is located in the region observed with the blue chip, showing a lower S/N. An example can be seen in the fit to star 235 shown in Fig. 4 (upper panel). The C abundances were adopted as upper limits.

The derived abundances are presented in Table 9. Beers & Christlieb (2005) defined carbon-enhanced metal-poor stars (CEMP) as having  $[\text{C}/\text{Fe}] > +1.0$ , but Aoki et al. (2007) presents a new definition, which takes into account the mixing events in evolved stars and the consequently lower carbon abundance on their surface. Following Aoki et al. (2005, 2007), we assumed the mass of the stars to be 0.8 M<sub>⊙</sub> to calculate the luminosities  $L/L_{\odot} \propto (M/M_{\odot})(g/g_{\odot})^{-1}(T_{\text{eff}}/T_{\text{eff}\odot})^4$ , and in Fig. 4 (lower panel) we show the  $[\text{C}/\text{Fe}]$  abundance ratios as a function of the luminosity  $\log(L/L_{\odot})$  for our sample. The limits for CEMP stars are also presented, showing that our sample consists of carbon-normal metal-poor stars (non-CEMP).

**Table 7.** Mean LTE abundances of the elements derived in the present work.

Element	A(X) <sub>⊙</sub>	A(X)	[X/Fe]	A(X)	[X/Fe]	A(X)	[X/Fe]	A(X)	[X/Fe]	A(X)	[X/Fe]
		221		224		230		235		238	
Fe I*	+7.50	+6.62	-0.88	+6.88	-0.62	+6.46	-1.04	+6.56	-0.94	+7.07	-0.43
Fe II*	+7.50	+6.59	-0.91	+6.90	-0.60	+6.47	-1.03	+6.55	-0.95	+7.08	-0.43
O I	+8.69	+8.40	+0.61	—	—	+8.25	+0.60	+8.40	+0.66	+8.85	+0.59
Na I	+6.24	+5.68	+0.33	+5.58	-0.06	+4.90	-0.31	+5.21	-0.09	+5.93	+0.12
Mg I	+7.60	+7.22	+0.52	+7.50	+0.51	+7.19	+0.63	+7.13	+0.47	+7.45	+0.28
Al I	+6.45	+6.00	+0.45	+6.29	+0.45	+5.77	+0.36	+5.79	+0.28	+6.23	+0.21
Si I	+7.51	+6.92	+0.31	+7.25	+0.35	+6.98	+0.50	+6.78	+0.22	+7.23	+0.14
Ca I	+6.34	+5.67	+0.23	+6.01	+0.28	+5.46	+0.16	+5.75	+0.36	+6.10	+0.18
Ti I	+4.95	+4.38	+0.33	+4.71	+0.37	+4.28	+0.37	+4.39	+0.39	+4.87	+0.34
Ti II	+4.95	+4.51	+0.46	+4.80	+0.46	+4.34	+0.42	+4.38	+0.38	+4.82	+0.30
Y I	+2.21	+1.60	+0.29	+1.95	+0.12	+1.90	+0.73	+1.60	+0.34	+1.92	+0.14
Zr I	+2.56	+2.40	+0.72	+2.60	+0.63	+2.40	+0.86	+2.33	+0.69	+2.60	+0.45
Ba II	+2.18	+1.60	+0.32	+1.80	+0.23	+1.63	+0.48	+1.90	+0.67	+2.10	+0.35
La II	+1.10	+0.30	+0.10	+1.03	+0.54	—	—	+0.68	+0.53	+0.90	+0.23
Eu II	+0.52	+0.00	+0.38	+0.35	+0.44	-0.10	+0.42	+0.05	+0.48	+0.56	+0.47

**Notes.** \*: [X/H] is used in place of [X/Fe].

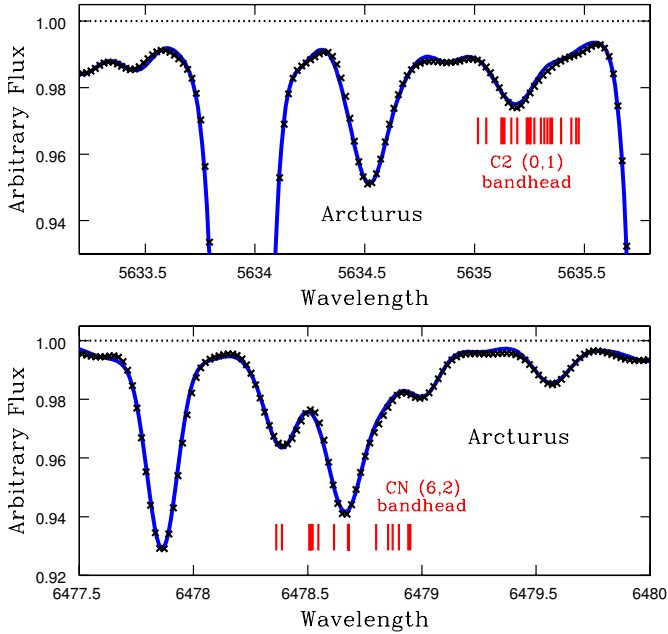


**Fig. 3. Upper panel:** Fit to the C<sub>2</sub>(1,0) molecular bandhead at 5635.3 Å in Arcturus. Observations (black crosses) are compared with synthetic spectra computed with the adopted abundances (blue solid lines) from literature. Red marks show the positions of molecular lines. **Lower panel:** Fit to the CN(6,2) molecular bandhead at 6478.5 Å in Arcturus. Symbols are the same as in the upper panel.

For comparison, we included carbon abundances of bulge stars from the literature. The open black squares represent seven stars in the globular cluster M 62 (NGC 6266) studied in high-resolution by Yong et al. (2014). This object is located at J(2000)  $\alpha = 17^h01^m12.60^s$  and  $\delta = -30^\circ06'44.5''$  (Di Criscienzo et al. 2006), or  $l = 353.5746^\circ$  and  $b = +7.3196^\circ$ , therefore projected in the bulge. The open black stars represent the results of the high-resolution abundance analysis from Barbuy et al. (2014) for the globular cluster NGC 6522, which is located at J(2000)  $\alpha = 18^h03^m34.08^s$  and  $\delta = -30^\circ02'02.3''$ , or  $l = 1.0246^\circ$  and

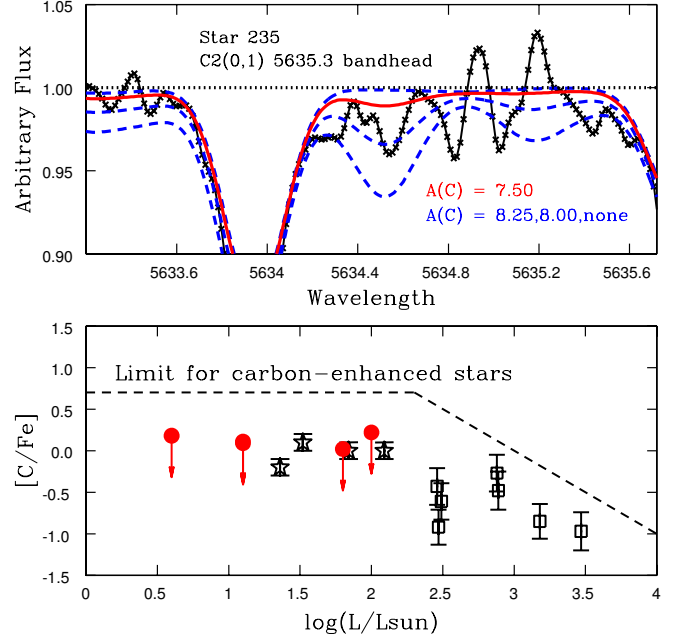


**Fig. 4. Upper panel:** Fit to the C<sub>2</sub>(1,0) bandhead at 5635.3 Å in star 235. Observations (black crosses) are compared with synthetic spectra computed with the different abundances indicated in the figure (blue dashed lines), as well as with the adopted abundance (red solid lines), also indicated. **Lower panel:** comparison of the [C/Fe] abundance ratios derived in the present sample (filled red circles) with stars from the bulge globular clusters M 62 (Yong et al. 2014, open black squares) and NGC 6522 (Barbuy et al. 2014, open black stars). The dashed black line corresponds to the limit for carbon-enhanced stars, as defined by Aoki et al. (2007).

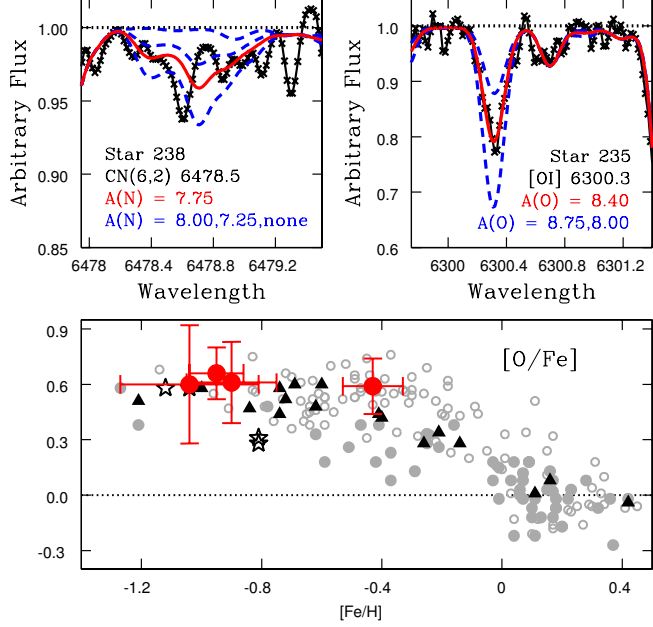
$b = -3.9256^\circ$  (Barbuy et al. 2009), and therefore also projected in the bulge.

The nitrogen abundance was derived using the CN A<sup>2</sup>Π - X<sup>2</sup>Σ red system, based on the CN(6, 2) 6478.48 Å bandhead. The CN line list is a compilation by B. Plez (private communication), using data from Cerny et al. (1978), Kotlar et al. (1980), Larsson



**Table 9.** Carbon and nitrogen abundances  $[X/Fe]$  from  $C_2$  and CN bandheads.

Species	$\lambda(\text{\AA})$	221	224	230	235	238
[C/Fe] $C_2(0, 1)$	5635.3	< +0.2	< +0.2	< +0.1	< 0.0	< +0.1
[N/Fe] $CN(6, 2)$	6478.5	+0.82	—	+0.71	+0.97	+0.35

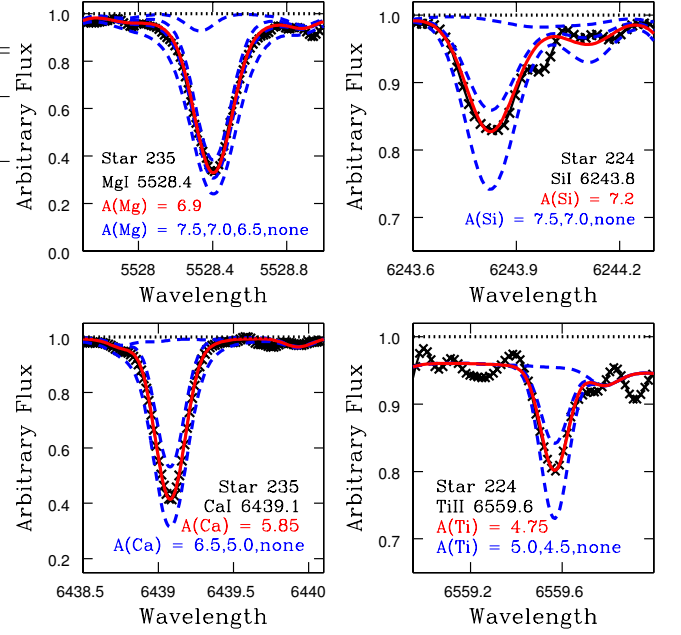

**Fig. 5.** Upper left panel: Fit to the CN(6,2) 6478.48 Å bandhead in star 238. Upper right panel: Fit to the [OI] 6300.3 Å line in star 235. Symbols are the same as in Fig. 4 (upper panel). Lower panel:  $[O/Fe]$  abundance ratio as a function of the metallicity for the five sample stars (filled red circles), compared with literature abundances from Bensby et al. (2013; filled black triangles), Barbuy et al. (2014; open black stars), Johnson et al. (2014; open grey circles), and Barbuy et al. (2015; filled grey circles).

et al. (1983), Bauschlicher et al. (1988), Ito et al. (1988a, 1988b), Prasad & Bernath (1992), Prasad et al. (1992), and Rehfuss et al. (1992). All four isotope combinations  $^{12}C^{14}N$ ,  $^{12}C^{15}N$ ,  $^{13}C^{14}N$ , and  $^{13}C^{15}N$  were treated with nitrogen solar isotopic fraction  $^{14}N$  (99.8%) and  $^{15}N$  (0.2%) from Asplund et al. (2009). The synthetic spectrum computed for Arcturus (blue solid line) in this region is shown in Fig. 3 (lower panel), showing good agreement with observations.

For the sample stars, the selected molecular transitions are weak and the noise becomes more evident, as shown in Fig. 5 (upper left panel) for star 238. Table 9 shows the derived N abundances which, owing to the previous discussion, must be used with caution. The difficulty in defining the local continuum does not permit us to determine the N abundance in the star 224.

## 5.2. Alpha elements

The oxygen abundance was derived using the forbidden line [OI] 6300.3 Å, as shown in Fig. 5 (upper right panel) for the star 235. We inspected the individual spectra, before combining, to check for possible blends with telluric lines, and we remove them from the final average when necessary. For star 224, the [OI] line was strongly contaminated in all individual spec-


**Fig. 6.** Upper left panel: Fit to the MgI 5528.4 Å line in star 235. Upper right panel: Fit to the SiI 6243.8 Å line in star 224. Lower left panel: Fit to the CaI 6439.1 Å line in star 235. Lower right panel: Fit to the TiII 6559.6 Å line in star 224. Symbols are the same as in Fig. 4 (upper panel).

tra, and consequently the oxygen abundance was not derived. Some individual spectra were also discarded owing to the higher noise level surrounding the [OI] line, compared with the average, which allowed a better placement of the continuum.

In Fig. 5 (lower panel) we compare the  $[O/Fe]$  abundance ratios in the sample stars with the result in the bulge globular cluster NGC 6522 (Barbuy et al. 2014), with microlensed bulge dwarfs and subgiants stars from Bensby et al. (2013) selected to have ages older than 11 Gyr, with selected red giant branch stars in the Galactic bulge from Johnson et al. (2014), and with the giant stars from Barbuy et al. (2015). The solar oxygen abundance  $A(O)_\odot = 8.69$  (Asplund et al. 2009) adopted in our results is 0.08 dex lower than  $A(O)_\odot = 8.77$  adopted in Barbuy et al. (2014, 2015) and, to ensure consistency among the abundance results, we shifted their values. This figure shows that our abundances are in agreement with previous results for bulge stars.

We checked four Mg I lines located at 5528.4 Å, 6318.7 Å, 6319.24 Å, and 6765.4 Å to derive the magnesium abundance. The line at 5528.4 Å is in the portion of the spectra with more noise, obtained with the blue chip, and was only useful in star 235, as shown in Fig. 6 (upper left panel). The silicon abundance was measured using ten Si I lines, two of them (5665.5 Å and 5690.4 Å) located in the wavelengths measured with the blue chip, but with individual abundances that are consistent with results from the lines in the red portion of the spectra. In the upper right panel of Fig. 6, we show the fit to the line at 6243.8 Å in star 224.

The calcium abundance was derived after checking 19 Ca I lines. The transition located at 5601.3 Å is the only line in the blue spectra and was used only for stars 235 and 238, giving individual abundances that are in agreement with the other lines. The result obtained from the Ca I 6439.1 Å line in star 235 is shown in Fig. 6 (lower left panel).

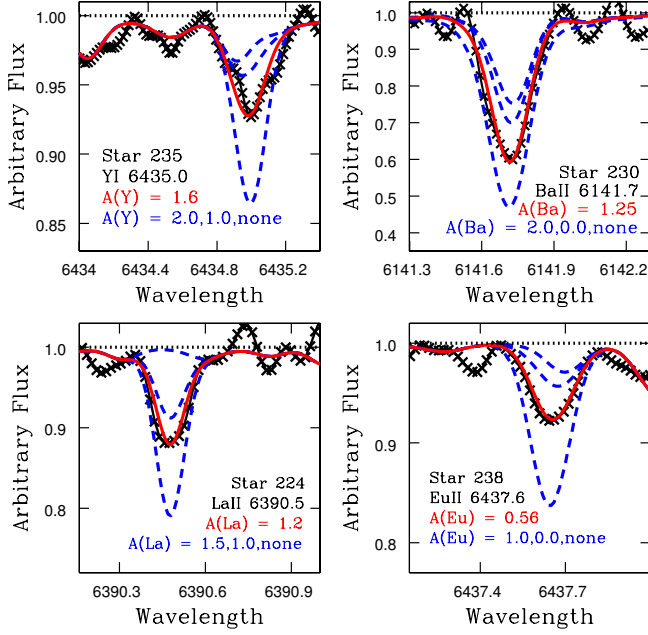


**Fig. 7.** Upper left panel: Fit to the Y I 6435.0 Å line in star 235. Upper right panel: Fit to the Ba II 6141.7 Å line in star 230. Lower left panel: Fit to the La II 6390.5 Å line in star 224. Lower right panel: Fit to the Eu II 6437.6 Å line in star 238. Symbols are the same as in Fig. 4 (upper panel).

It was possible to inspect 14 Ti I lines, with only the Ti I 5689.5 Å line located in the blue portion of the spectra. For the ionized species, six Ti II lines were checked to obtain the titanium abundance, but three of them (5336.8 Å, 5381.0 Å, and 5418.7 Å) are located in wavelengths of the blue portion of the spectra and they were only used for stars 235 and 238. In the lower right panel of Fig. 6, we show the Ti II 6559.6 Å line measured in star 224. This line is located in the blue wing of the H $\alpha$  line, and it was necessary to take the hydrogen line in the spectrum synthesis into account.

### 5.3. Odd-Z elements Na, Al

The sodium abundances are based on four Na I lines, located at 4982.8 Å, 5688.2 Å, 6154.2 Å, and 6160.7 Å. We did not use the resonance lines Na I 5889.95 Å (D2) and Na I 5895.92 Å (D1) because they are very sensitive to non-LTE effects. The only stable isotope  $^{23}\text{Na}$  has nuclear spin  $I = 3/2$  and therefore exhibits hyperfine structure (HFS). The hyperfine coupling constants are adopted from Das & Natarajan (2008) and Marcassa et al. (1998). When not available in the literature, the hyperfine constants for a given level were assumed to be null. The line splitting was computed by employing a code made available by McWilliam et al. (2013).

For aluminum, only Al I 6696.0 Å and Al I 6698.7 Å lines were available. The stable isotope  $^{27}\text{Al}$  has nuclear spin  $I = 5/2$  and we adopted the hyperfine coupling constants from Nakai et al. (2007) and Belfrage et al. (1984) to compute the HFS.

<sup>2</sup> Adopted from the Particle Data Group (PDG) collaboration: <http://pdg.lbl.gov/>

### 5.4. Heavy elements

We derive the abundances of the neutron-capture elements Y, Zr, Ba, La, and the reference r-element Eu. We preferentially used lines of ionized species, since these elements are mostly in this form. For strontium, we evaluated six Sr I lines: 6408.5 Å, 6504.0 Å, 6546.8 Å, 6550.2 Å, 6617.3 Å, and 6791.0 Å. All transitions are too weak for abundance purposes, consequently no [Sr/Fe] result is presented.

The best yttrium line Y II 6795.4 Å is located in the border of the échelle spectrum and shows clearly fringes that prevent its use. The most reliable line from our spectra is Y II 5544.6 Å, which is located in the blue portion of the spectra and was not useful for the abundance determination. Consequently, the Y abundance in the sample is based on the Y I 6435.0 Å line, as shown in the upper left panel of Fig. 7 for star 235.

For zirconium, we checked three Zr II lines located at 5112.3 Å, 5350.1 Å, and 5350.3 Å, but none is reliable for measuring abundances. Due to a lack of useful ionized lines, we measured abundances from three lines of Zr I: 6127.47 Å, 6134.58 Å, and 6143.25 Å. Oscillator strengths were adopted from van der Swaelmen et al. (2013).

The barium abundance was measured using the Ba II 6141.7 Å and Ba II 6496.9 Å lines. As well known, the HFS (nuclear spin  $I = 3/2$ ) and the isotopic splitting are important effects to be taken into account in Ba transitions. Following Barbuy et al. (2014), the hyperfine coupling constants were adopted experimentally from Rutten (1978) and Biehl (1976). According to Asplund et al. (2009), the major contribution comes from the isotope  $^{138}\text{Ba}$  (71.698%), followed by  $^{137}\text{Ba}$  (11.232%),  $^{136}\text{Ba}$  (7.854%),  $^{135}\text{Ba}$  (6.592%), and  $^{134}\text{Ba}$  (2.417%). The isotopes  $^{130}\text{Ba}$  and  $^{132}\text{Ba}$  together represent less than 0.11% and they were ignored in the computations. In addition, to compute the profile for Ba II 6141.7 Å, it is important to include a blend with the Fe I 6141.7 Å, for which we adopted  $\log gf = -1.60$  (Barbuy et al. 2014). The fit to this line for star 230 is shown in Fig. 7 (upper right panel).

The lanthanum abundance is a contribution of two stable isotopes. The most relevant is  $^{139}\text{La}$ , with 99.909% in the solar material, and the only isotope included in the computations since  $^{138}\text{La}$  contributes less than 0.1% (Asplund et al. 2009). The HFS values were computed with coupling constants A and B adopted from Lawler et al. (2001a) and Biehl (1976), with nuclear spin  $I = 7/2$ . The final abundances are based on three La II lines, located at 6320.4 Å, 6390.5 Å, and 6774.3 Å. In Fig. 7 we show the fit to the La II 6320.5 Å line for star 224 (lower left panel).

Europium is the heaviest element measured in the sample stars. The solar isotopic fraction  $^{151}\text{Eu} = 47.81\%$  and  $^{153}\text{Eu} = 52.19\%$  (Asplund et al. 2009) was adopted, with nuclear spin  $I = 5/2$ . We computed the HFS using coupling constants A and B from Lawler et al. (2001b). The final europium abundances were derived from the Eu II 6437.6 Å and Eu II 6645.1 Å lines, and in Fig. 7 we show (lower right panel) the result for the Eu II 6437.6 Å line in star 238.

### 5.5. Uncertainties on the derived abundances

The typical errors in the spectroscopic atmospheric parameters are  $\Delta T_{\text{eff}} = 100$  K,  $\Delta \log g = 0.1$  dex, and  $\Delta \xi = 0.2$  km s $^{-1}$ . Since the stellar parameters are not independent, the quadratic sum of the abundance uncertainties that arise from each of these three sources independently will add significant covariance terms to the final error budget.



**Table 10.** Observational and atmospheric errors in star 235, as well as the final uncertainties.

Element	$\Delta_{obs}$	$\Delta_{atm}$	$\Delta_{final(X/H)}$	$\Delta_{final(X/Fe)}$
	(dex)	(dex)	(dex)	(dex)
Fe I	0.15	0.08	0.17	—
Fe II	0.09	0.06	0.11	—
C(C <sub>2</sub> )	0.09	0.04	0.10	0.14
N(CN)	0.09	0.14	0.17	0.19
[O I]	0.09	0.12	0.15	0.18
Na I	0.09	0.02	0.09	0.14
Mg I	0.09	0.03	0.09	0.14
Al I	0.09	0.05	0.10	0.14
Si I	0.03	0.02	0.04	0.11
Ca I	0.10	0.02	0.10	0.14
Ti I	0.06	0.08	0.10	0.14
Ti II	0.04	0.07	0.08	0.13
Y I	0.09	0.07	0.11	0.15
Zr I	0.09	0.08	0.12	0.16
Ba II	0.09	0.02	0.09	0.14
La II	0.09	0.07	0.11	0.15
Eu II	0.09	0.05	0.10	0.14

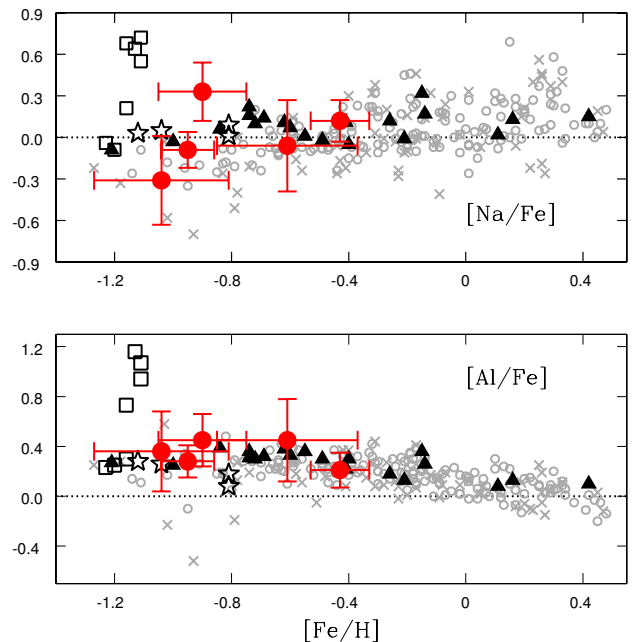
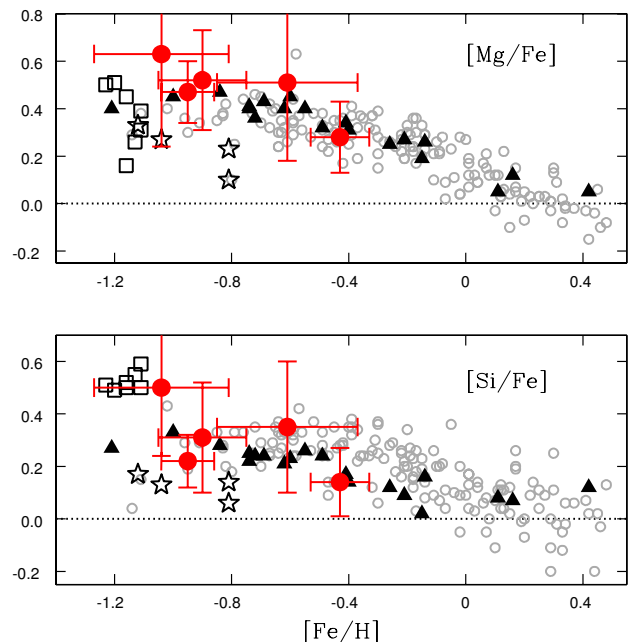
We solved this problem by creating a new atmospheric model with a 100 K lower temperature, determining the corresponding surface gravity  $\log g$  and microturbulent velocity  $\xi$  by the spectroscopic method. The difference between the abundances derived with this new model and the nominal model in each star are expected to represent the total error budget arising from the stellar parameters.

The observational uncertainties are assumed as the standard error of the mean obtained with the abundances from individual lines. For elements with three or less lines used to determine the average, we adopted the Fe observational error as a representative value. The final error is the quadratic sum of the uncertainty from the atmospheric parameters and the observational error. Table 10 shows the results in star 235 as an example. It is important to note, as described already in Table 6, that the observation errors in stars 221, 224, and 230 are significantly larger in comparison with stars 235 and 238, as a consequence of differences in the S/N.

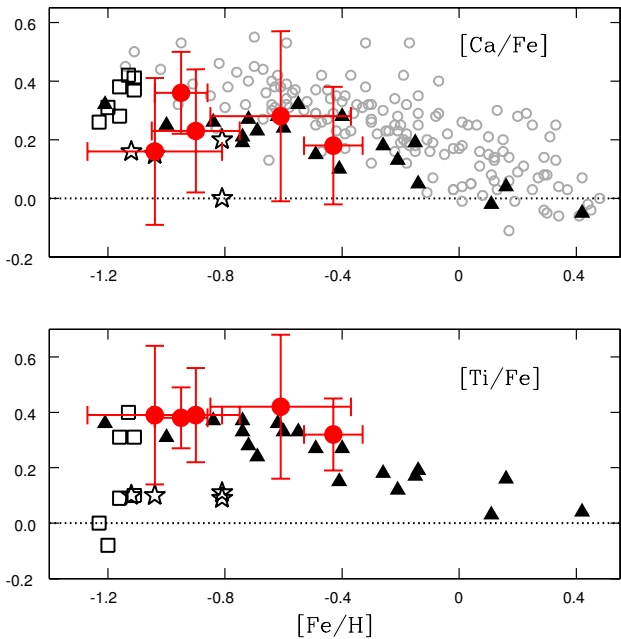
## 6. Discussion

The sample stars analysed at high spectral resolution are confirmed to be moderately metal-poor with  $-1.04 \leq [\text{Fe}/\text{H}] \leq -0.43$  with no enhancement in  $[\text{C}/\text{Fe}]$ , and some stars show high nitrogen abundances  $[\text{N}/\text{Fe}]$ :  $+0.82 \pm 0.26$ ,  $+0.71 \pm 0.34$ ,  $+0.97 \pm 0.19$ , and  $+0.35 \pm 0.20$ , for 221, 230, 235, and 238, respectively.

In the context of APOGEE (Majewski et al. 2015), Schiavon et al. (2015) recently reported the discovery of a population of Galactic bulge field stars with high values of  $[\text{N}/\text{Fe}]$ , which is correlated with  $[\text{Al}/\text{Fe}]$  and anticorrelated with  $[\text{C}/\text{Fe}]$ , typical of globular cluster stars (Hesser et al. 1982; Gratton, Carretta & Bragaglia 2012). The N-rich stars in our sample could be related to the population newly discovered by Schiavon et al. (2015). According to the authors, abundance ratios  $[\text{N}/\text{Fe}] > +0.6$  cannot be explained by the CN-cycle mixing scenario, and the contamination by mass transfer binaries mechanism can only account for, at most, 25% of their sample. Possible scenarios for the origin of the N-rich stars are: i) dissolution of an early population of globular clusters (Belokurov et al. 2006; Shapiro et


**Fig. 8.**  $[\text{Na}/\text{Fe}]$  (upper panel) and  $[\text{Al}/\text{Fe}]$  (lower panel) abundance ratios as a function of the metallicity for the five sample stars (filled red circles), compared with literature abundances from Yong et al. (2014; open black squares), Barbuy et al. (2014; open black stars), Bensby et al. (2013; filled black triangles), Johnson et al. (2012; grey crosses), and Johnson et al. (2014; open grey circles).

**Fig. 9.**  $[\text{Mg}/\text{Fe}]$  (upper panel) and  $[\text{Si}/\text{Fe}]$  (lower panel) abundance ratios as a function of the metallicity for the five sample stars, compared with literature abundances. Symbols are the same as in Fig. 8.

al. 2010; Kruijssen 2015; Bournaud 2016); ii) a shared (or similar) molecular cloud responsible for forming these stars and the globular cluster (Longmore et al. 2014; Schiavon et al. 2015); iii) these stars are among the oldest in the Galaxy and their abun-



**Fig. 10.**  $[\text{Ca}/\text{Fe}]$  (upper panel) and  $[\text{Ti}/\text{Fe}]$  (lower panel) abundance ratios as a function of the metallicity for the five sample stars, compared with literature abundances. Symbols are the same as in Fig. 8.

dances are imprints of the first stellar generations (Tumlinson 2010; Chiappini et al. 2011).

To better place our results in the context of the Galactic bulge, we present comparisons with literature abundances in bulge stars. As already described in Sect. 5.1, we adopted results from Yong et al. (2014) of seven stars in the globular cluster M 62, the ninth most luminous Galactic globular cluster, which also presents an extended horizontal branch. The stars were observed with the High Dispersion Spectrograph (HDS; Noguchi et al. 2002) on the Subaru Telescope and with the Magellan Inamori Kyocera Echelle spectrograph (MIKE; Bernstein et al. 2003) at the Magellan-II Telescope. The authors found a good agreement between the scaled-solar r-process distribution and the derived abundances for the elements heavier than La, as well as an enhancement in Y, Zr, and Ba in comparison with the solar r-process pattern. According to Yong et al. (2014), these results are incompatible with the s-process in AGB stars and suggest the fast-rotating massive stars as a possible solution.

Also discussed in Sect. 5.1, Barbuy et al. (2014) analysed four stars in the globular cluster NGC 6522, which appears to be the oldest known Milky Way globular cluster. The targets were observed at the VLT using the UVES spectrograph (Dekker et al. 2000) in FLAMES-UVES mode. They found an enhancement in s-process-dominant elements, suggesting spinstars as a possibility to form these elements, besides the usual explanations of mass transfer from s-process-rich AGB stars and extra mechanisms as the weak r-process as possible scenarios to explain the abundance signatures. Ness et al. (2014) found similar results to Barbuy et al. (2014), but these authors insist that the abundances of this cluster were measured to be similar to bulge field stars, halo stars, and other Galactic globular clusters of the same metallicity. We note that NGC 6522 appears to be among the oldest globular clusters, and as such it should show signatures as one of the main pieces of the sub-systems that first formed in the central parts of the Galaxy.

In addition, we selected 62 red giant stars analysed in Johnson et al. (2012), observed in Plaut’s low-extinction window. Using the Hydra multi-fiber spectrograph on the CTIO Blanco 4 m telescope, the stars were observed at  $l = -1^\circ$  and  $b = -8.5^\circ$  (field 1) and at  $l = 0^\circ$  and  $b = -8^\circ$  (field 2). Another 156 red giant branch stars in two Galactic bulge fields centred near  $l = +5.25^\circ$  and  $b = -3.02^\circ$  and  $l = 0^\circ$  and  $b = -12^\circ$  analysed in Johnson et al. (2014), using FLAMES-GIRAFFE spectra, were selected in the comparison.

In Bensby et al. (2013), 58 microlensed bulge dwarfs and subgiants stars were analysed. The authors estimated the stellar ages based on isochrones (Demarque et al. 2004) and probability distribution functions (Bensby et al. 2011), so we selected 22 stars with ages older than 11 Gyr, avoiding the younger stellar populations present in the bulge.

Finally, 56 other bulge giant stars were selected from Van der Swaelmen et al. (2016), who analysed the heavy elements in this sample. Already studied in Zoccali et al. (2006), Lecœur et al. (2007), and Barbuy et al. (2013, 2015), the observations were performed with the multi-fibre spectrograph FLAMES-UVES, at the UT2 Kuyen VLT/ESO telescope. The stars are located at the Baade’s Window ( $l = 1.14^\circ$ ,  $b = -4.2^\circ$ ), at the Blanco field ( $l = 0^\circ$ ,  $b = -12^\circ$ ), at the field of NGC 6553 ( $l = 5.2^\circ$ ,  $b = -3^\circ$ ), and in an additional field at  $l = 0.2^\circ$  and  $b = -6^\circ$ .

In Fig. 8 we show the comparisons for the odd-Z elements sodium (upper panel) and aluminum (lower panel), while the  $\alpha$ -elements Mg, Si, Ca, and Ti are presented in Figs. 9 and 10. As a general behaviour, the derived abundances in the sample stars are in agreement with the literature, for objects with the same metallicities, within the error bars. Chemical similarities between globular cluster primary stellar populations and field stars for a given metallicity were studied in other works (see e.g. Renzini 2008; Gratton et al. 2012; Schiavon et al. 2015).

Chemical inhomogeneity among stars within individual globular clusters are well known for elements like C, N, O, Na, Mg, and Al (see Kraft 1994; Gratton et al. 2004, 2012; Mészáros et al. 2015), and several models are claimed to explain this observational signature (Fenner et al. 2004; Decressin et al. 2007; Renzini 2008; Marcolini et al. 2009; Hopkins 2014; Renzini et al. 2015). To test these so-called abundance anomalies, we checked if the Na – O, Al – O, and Al – Mg anticorrelations were present in our sample, as well as the Na – Al correlation, but no significant trend was found. The  $\alpha$ -elements abundances are enhanced, as typical of chemical enrichment from core-collapse supernovae (Woosley & Weaver 1995; Nomoto et al. 2013, and references therein).

Regarding the heavy elements, we derived abundances of Y, Zr, Ba, La, and Eu in our sample, and, in Figs. 11 and 12, we show the results in comparison to values from literature. A good agreement is observed among the selected stars and, analogously to  $\alpha$ -elements, enhancement in the heavy elements was obtained in the sample. The only exception to this average behaviour in literature is observed in Bensby et al. (2013), for which the major fraction of stars shows solar values of  $[\text{Y}/\text{Fe}]$  and  $[\text{Ba}/\text{Fe}]$  abundance ratio.

The behaviour of the  $[\text{Eu}/\text{Fe}]$  abundance ratio is similar with that observed for the  $\alpha$ -elements, which would be expected from the main r-process. In the solar material, the r-process is responsible for  $94 \pm 0.4\%$  of the total Eu abundance (Bisterzo et al. 2014). However, most of the Y, Zr, Ba, and La available today in the solar system and in the Galaxy has been produced by the s-process in low-mass AGB stars (Snedden et al. 2008, and references therein) which, owing to the typical long lifetimes of low-mass stars, would not have had time to evolve and pollute

the gas before forming the sample stars, which are probably very old. Possible scenarios for the enrichment of Y, Zr, Ba, and La derived in our sample are:

i) Early enrichment from r-process only, where an extra mechanism is required to produce excesses of the lightest trans-Fe elements with respect to second peak elements such as Ba and La (e.g. Travaglio et al. 2004; Wanajo et al. 2011; Arcones & Montes 2011; Arcones & Thielemann 2013; Fujibayashi et al. 2015; Niu et al. 2015);

ii) s-process elements from AGB stars bounded in a binary system, polluting the observed stars via AGB-mass transfer (Bisterzo et al. 2014);

iii) s-process activation in early generations of Spinstars (Meynet et al. 2006; Pignatari et al. 2008; Frischknecht et al. 2012; Frischknecht et al. 2015), which pollutes the primordial material before forming the oldest bulge field stars.

Figure 13 shows the  $[Y/Ba]$  vs.  $[Fe/H]$  diagram for bulge stars from our sample compared with selected results from the literature. From Bensby et al. (2013), we only retained the star enhanced in  $[Y/Fe]$ . We included the average  $[Y/Ba]_r = -0.42 \pm 0.12$  abundance ratio value obtained (yellow region) from six halo metal-poor r-element-rich stars (HD 221170, HD 115444, CB 22892-052, HE 1523-0901, BD 17 3248, and CS 31082-001), compiled in Sneden et al. (2008), as a representative value of the main r-process. We also show the mean value of the  $[Y/Ba]$  ratio obtained from six halo metal-poor r-process stars showing enhancement in the lightest heavy elements: HD 88609 (Honda et al. 2007), BD 4 2621 (Johnson 2002), HD 4306 (Honda et al. 2004), HD 237846 (Roederer et al. 2010), HD 122563 (Honda et al. 2007), and HD 140283 (Siqueira-Mello et al. 2015). The average value is  $[Y/Ba]_E = +0.56 \pm 0.18$  (illustrated in the figure by the cyan region - where E stands for “enhanced”). The source of this enhancement can be manifold (see discussion below). We note that the cyan region is meant to only show a reference value since, even for the same nucleosynthetic sources, the expected level of enhancement in the bulge and halo will be different (see Barbuy et al. 2014).

The figure shows that the value derived in star 235 agrees with those observed in the r-element-rich stars, and it can be explained by a pattern arising in a so-called main r-process. Considering the error bars, the same conclusion could be claimed to explain the  $[Y/Ba]$  abundance in star 238. On the other hand, the derived abundances in 221, 224, and 230 are barely explained using only the main r-process. If the bulge stars with  $[Fe/H] \sim -1$  trace the same early phases of chemical enrichment as halo stars with  $[Fe/H] \sim -3$ , the sample stars 235 and 238 may be classified as r-process enhanced stars, analogous to the r-I and r-II metal-poor halo stars (Beers & Christlieb 2005). In fact, using the latter authors’ definitions that are based on the  $[Ba/Eu]$  abundance ratio, objects 235 and 238 must be classified as r/s and r-I stars, respectively. This is the first time that these kind of stars are identified in the Galactic bulge.

Figure 14 presents the same comparison for zirconium. In the upper panel the  $[Zr/Fe]$  abundance ratios derived in the sample are compared with results from the literature. Johnson et al. (2012) identified evidence of two separate sequences: a group of stars enhanced in  $[Zr/Fe]$ , and another group moderately poor. Clearly our sample stars are members of the enhanced group. In the lower panel we show the  $[Zr/Ba]$  vs.  $[Fe/H]$  diagram for the sample stars and the selected results from literature. The selected metal-poor r-element-rich and the enhanced stars in lightest heavy elements were also used to define  $[Zr/Ba]_r = -0.18 \pm 0.12$  (yellow region) and  $[Zr/Ba]_E = +0.95 \pm 0.15$  (cyan region), respectively. The figure shows that the Zr abundances derived

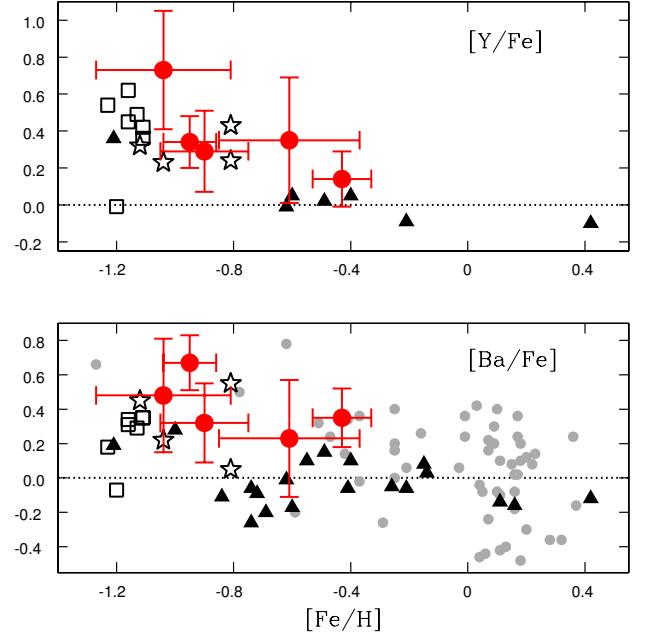


**Fig. 11.**  $[Y/Fe]$  (upper panel) and  $[Ba/Fe]$  (lower panel) abundance ratios as a function of the metallicity for the five sample stars, compared with literature abundances. Symbols are the same as in Fig. 8, in addition to the abundances from Van der Swaelmen et al. (2016; filled grey circles).

in stars 235 and 238 also agree with those observed in the r-element-rich stars, while stars 221, 224, and 230 require extra mechanism(s) to explain the abundance ratios.

For the Galactic halo, Roederer et al. (2010) show several metal-poor stars located in the region between these two extremes abundance regimes, suggesting also a continuous range of r-process nucleosynthesis patterns. On the other hand, Niu et al. (2015) more recently suggest that the weak r-process and the main r-process are two distinct astrophysical processes.

The fundamental challenge that we are facing is that in the early galaxy a multitude of different nucleosynthesis processes may have contributed to the production of the elements at the first neutron-magic peak beyond iron, including Sr, Y, and Zr. Together with the s-process in fast rotating massive stars (Frischknecht et al. 2016) and the weak r-process (e.g., Farouqi et al. 2009), other sources could be at play such as: the electron capture supernovae (e.g., Wanajo et al. 2011), or the  $\alpha$ -rich freezeout in most energetic core-collapse supernovae (e.g., Woosley & Hoffman 1992), and the intermediary neutron capture i-process (Dardelet et al. 2015, and references therein). In addition, neutrino-winds in core-collapse supernovae can host a large variety of processes that can produce elements in the same mass region (e.g., Fröhlich et al. 2006, Farouqi et al. 2010, Roberts et al. 2010, Arcones & Montes 2011). It is thus crucial to measure as many heavy elements as possible to isolate the different nucleosynthesis sources.

## 7. Conclusions

We have carried out a pilot project with the goal of providing detailed abundances for moderately metal-poor Galactic bulge stars that are believed to host imprints left by the first stellar generations. In this work, we were able to obtain detailed abundances for five moderately metal-poor and  $[\alpha/Fe] > 0$  stars from

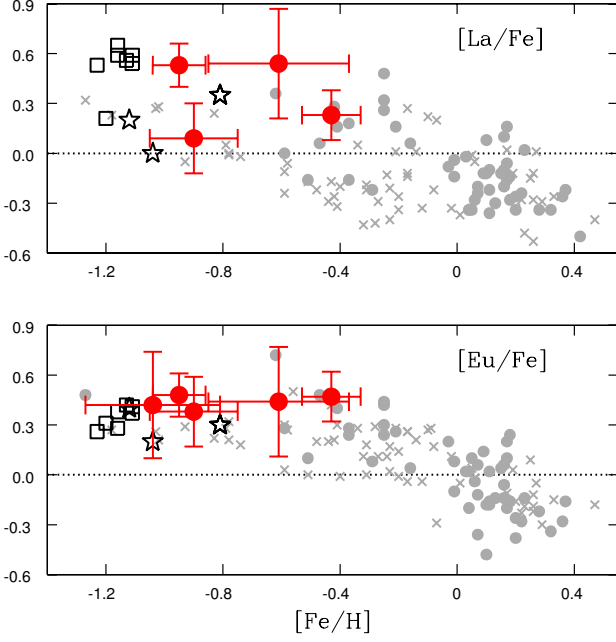


**Fig. 12.**  $[\text{La}/\text{Fe}]$  (upper panel) and  $[\text{Eu}/\text{Fe}]$  (lower panel) abundance ratios as a function of the metallicity for the five sample stars, compared with literature abundances. Symbols are the same as in Figs. 8 and 11.

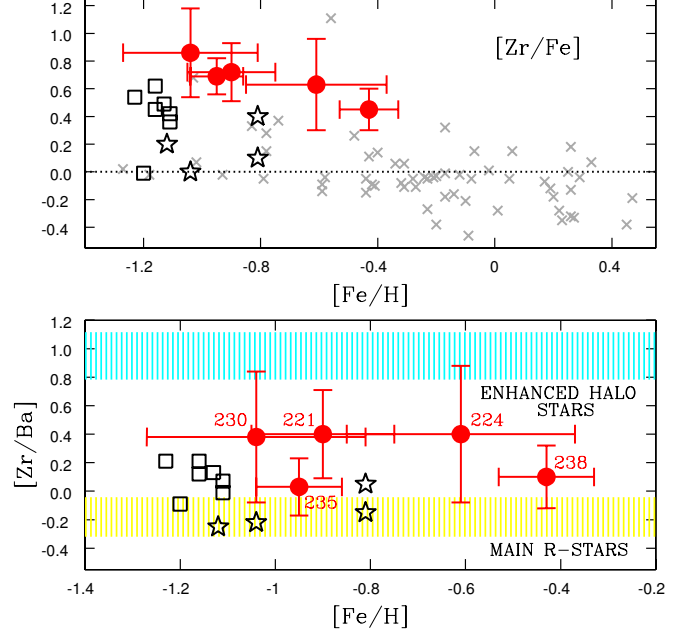


**Fig. 14.** Upper panel:  $[\text{Zr}/\text{Fe}]$  abundance ratios as a function of the metallicity for the five sample stars, compared with literature abundances. Symbols are the same as in Figs. 8. Lower panel:  $[\text{Zr}/\text{Ba}]$  vs.  $[\text{Fe}/\text{H}]$  diagram for the sample stars and results from literature. Symbols are the same as in Figs. 8. The yellow and cyan regions correspond to the main r-process signature and the abundance ratio from metal-poor stars enhanced in the lightest heavy elements (see text for details).

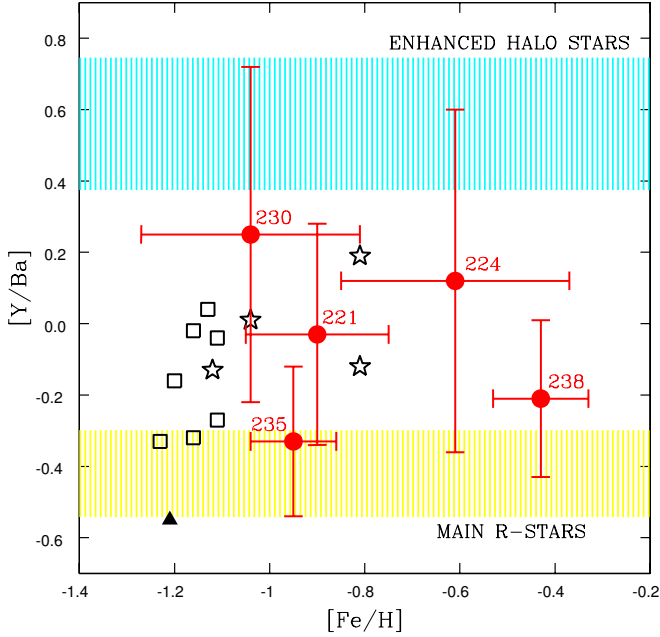


**Fig. 13.**  $[\text{Y}/\text{Ba}]$  vs.  $[\text{Fe}/\text{H}]$  diagram for the sample stars and results from literature. Symbols are the same as in Figs. 8. The yellow and cyan regions correspond to the main r-process signature and the abundance ratio from metal-poor stars enhanced in the lightest heavy elements (see text for details).

one field of the ARGOS survey. Our high-resolution FLAMES-UVES spectra have confirmed three out of five stars to have metallicities  $[\text{Fe}/\text{H}] < -0.8$ . All stars are confirmed to be  $\alpha$ -enhanced: overabundances of the typical  $\alpha$ 's Mg, Si, Ca, Ti, and of the odd-Z element Al are clearly detected.

Three sample stars exhibit high  $[\text{N}/\text{Fe}]$  abundance ratios. Similar high- $[\text{N}/\text{Fe}]$  bulge stars were recently found in APOGEE (see Schiavon et al. 2015). According to the latter authors, abundance ratios  $[\text{N}/\text{Fe}] > +0.6$  cannot be explained by the CN-cycle mixing scenario.

The sample stars show enhancements in  $[\text{Y}/\text{Fe}]$ ,  $[\text{Zr}/\text{Fe}]$ ,  $[\text{Ba}/\text{Fe}]$ ,  $[\text{La}/\text{Fe}]$ , and  $[\text{Eu}/\text{Fe}]$ . We found that three of our stars also show  $[\text{Y}/\text{Ba}]$  and  $[\text{Zr}/\text{Ba}]$  ratios slightly higher than expected from a pure main r-process nucleosynthesis. These results are very similar to the recent reported chemical pattern found in some stars of the oldest Milky Way globular cluster, NGC 6522 (Barbuy et al. 2014). Considering the sample stars as an old population, whereas an enhancement in Eu would be expected from the rapid neutron capture process (or r-process), consistent with the observed  $[\alpha/\text{Fe}]$  enhancements, the observed anomalous enrichment of the dominantly s-process elements  $[\text{Y}/\text{Ba}]$  and  $[\text{Zr}/\text{Ba}]$  in these stars are more difficult to understand using standard nucleosynthesis processes.

Finally, previous to the present work, some excesses of s-process-typical elements in the Galactic bulge had been found only in globular clusters (Barbuy et al. 2009; Chiappini et al. 2011; Barbuy et al. 2014; Yong et al. 2014). The goal of our pilot project was to also look for the existence of these stars in the field. Although our sample is very small, three of our stars seem to show not only excesses of the lightest heavy elements with respect to iron, but also enhancement in the  $[\text{Y}/\text{Ba}]$  and  $[\text{Zr}/\text{Ba}]$  abundance ratios. The s-process activation in fast-rotating massive stars and/or other extra mechanisms are possible solutions to these anomalies. There is a debate in the literature about the origin of heavy elements in the oldest stars, such that future large samples are urgently needed to further explore the impact of these



findings in our understanding of the nature of the first stellar generations.

*Acknowledgements.* CS, BB, and EC acknowledge grants from CAPES, CNPq and FAPESP. MP acknowledges support from NSF grants PHY 02-16783 and PHY 09-22648 (Joint Institute for Nuclear Astrophysics, JINA), NSF grant PHY-1430152 (JINA Center for the Evolution of the Elements) and EU MIRG-CT-2006-046520. The continued work on codes and in disseminating data is made possible through funding from STFC and EU-FP7-ERC-2012-St Grant 306901 (RH, UK). MP acknowledges support from the Lendulet-2014 Programme of the Hungarian Academy of Sciences and from SNF (Switzerland). The research leading to these results has received funding from the European Research Council under the European Union's Seventh Framework Programme (FP/2007-2013) / ERC Grant Agreement n. 306901. R. Hirschi acknowledges support from the World Premier International Research Center Initiative (WPI Initiative), MEXT, Japan. This work has made use of the VALD database, operated at Uppsala University, the Institute of Astronomy RAS in Moscow, and the University of Vienna.

## References

- Alonso, A., Arribas, S., Martínez-Roger, C. 1998, *A&AS*, 131, 209  
 Alonso, A., Arribas, S., Martínez-Roger, C. 1999, *A&AS*, 140, 261  
 Alvarez, R. & Plez, B. 1998, *A&A*, 330, 1109  
 Anstee, S. D. & O'Mara, B. J. 1995, *MNRAS*, 276, 859  
 Aoki, W., Honda, S., Beers, T. C. et al. 2005, *ApJ*, 632, 611  
 Aoki, W., Beers, T. C., Christlieb, N. et al. 2007, *ApJ*, 655, 492  
 Arcones, A. & Montes, F. 2011, *ApJ*, 731, 5  
 Arcones, A. & Thielemann, F.-K. 2013, *JPhG*, 40, 013201  
 Asplund, M., Grevesse, N., Sauval, A. J. et al. 2009, *ARA&A*, 47, 481  
 Ballester, P., Modigliani, A., Boitquin, O. et al. 2000, *Msngr*, 101, 31  
 Barbuy, B., Zoccali, M., Ortolani, S. et al. 2009, *A&A*, 507, 405  
 Barbuy, B., Hill, V., Zoccali, M. et al. 2013, *A&A*, 559, A5  
 Barbuy, B., Chiappini, C., Cantelli, E. et al. 2014, *A&A*, 570, A76  
 Barbuy, B., Friaça, A. C. S., da Silveira, C. R. et al. 2015, *A&A*, 580, A40  
 Barklem, P. S. & O'Mara, B. J. 1997, *MNRAS*, 290, 102  
 Barklem, P. S., O'Mara, B. J., Ross, J. E. 1998, *MNRAS*, 296, 1057  
 Bauschlicher, C. W., Jr., Langhoff, S. R., Taylor, P. R. 1988, *ApJ*, 332, 531  
 Beers, T. C. & Christlieb, N. 2005, *ARA&A*, 43, 531  
 Belfrage, Ch., Hörbäck, S., Levinson, C. et al. 1984, *ZPhyA*, 316, 15  
 Belokurov, V., Evans, N.W., Irwin et al. 2006, *ApJ*, 637, L29  
 Bensby, T., Adén, D., Meléndez, J. et al. 2011, *A&A*, 533, A134  
 Bensby, T., Yee, J.C., Feltzing, S. et al. 2013, *A&A*, 549, A147  
 Bernstein, R., Shectman, S. A., Gunnels, S. M. et al. 2003, *SPIE*, 4841, 1694  
 Bessell, M. S., Castelli, F., Plez, B. 1998, *A&A*, 333, 231  
 Biehl, D. 1976, Ph.D. Thesis, Kiel University, Germany  
 Bisterzo, S., Gallino, R., Straniero, O. et al. 2010, *MNRAS* 404, 1529  
 Bisterzo, S., Travaglio, C., Gallino, R., et al. 2014, *ApJ*, 787, 10  
 Bournaud, F. 2016, *ASSL*, 418, 355  
 Carpenter, J. 2001, *AJ*, 121, 2851  
 Castelli, F., Kurucz, R. L. 2004, arXiv:astro-ph/0405087  
 Cerny, D., Bacis, R., Guelachvili, G. et al. 1978, *JMoSp*, 73, 154  
 Chiappini, C., Frischknecht, U., Meynet G., et al. 2011, *Nature* 474, Issue 7353, pp. 666  
 Cowan, J. J. & Rose, W. K. 1977, *ApJ*, 212, 149  
 Dardelet, L., Ritter, C., Prado, P. et al. 2015, arXiv:1505.05500  
 Das, D. & Natarajan, V. 2008, *J. Phys. B*, 41, 5001  
 Decressin, T., Meynet, G., Charbonnel, C. et al. 2007, *A&A*, 464, 1029  
 Dekker, H., D'Odorico, S., Kaufer, A. et al. 2000, *SPIE*, 4008, 534  
 Demarque, P., Woo, J.-H., Kim, Y.-C. et al. 2004, *ApJS*, 155, 667  
 Di Criscienzo, M., Caputo, F., Marconi, M. et al. 2006, *MNRAS*, 365, 1357  
 Farouqi, K., Kratz, K.-L., Mashonkina, L. I. et al. 2009, *ApJ*, 694, 49  
 Farouqi, K., Kratz, K.-L., Pfeiffer, B. et al. 2010, *ApJ*, 712, 1359  
 Fenner, Y., Campbell, S., Karakas, A. I. et al. 2004, *MNRAS*, 353, 789  
 Freeman, K., Ness, M., Wylie-de-Boer, E. et al. 2013, *MNRAS*, 428, 3660  
 Frischknecht, U., Hirschi, R., Thielemann, F.-K. 2012, *A&A*, 538, L2  
 Frischknecht et al. 2015, submitted  
 Fröhlich, C., Martínez-Pinedo, G., Liebendörfer, M. et al. 2006, *PhRvL*, 96, 142502  
 Fujibayashi, S., Yoshida, T. & Sekiguchi, Y. 2015, *ApJ*, 810, 115  
 Gratton, R. G., Snenen, C. & Carretta, E. 2004, *ARA&A*, 42, 385  
 Gratton, R. G., Carretta, E. & Bragaglia, A. 2012, *A&AR*, 20, 50  
 Grieco, V., Matteucci, F., Pipino, A. et al. 2012, *A&A*, 548, A60  
 Gustafsson, B., Edvardsson, B., Eriksson, K. et al. 2008, *A&A*, 486, 951  
 Hesser, J. E., Bell, R. A., Harris, G. L. H. & Cannon, R. D. 1982, *AJ*, 87, 1470  
 Hinkle, K., Wallace, L., Valenti, J., Harmer, D. 2000, *Visible and Near Infrared Atlas of the Arcturus Spectrum 3727-9300 Å*, ed. K. Hinkle, L. Wallace, J. Valenti, and D. Harmer (San Francisco: ASP)  
 Honda, S., Aoki, W., Kajino, T. et al. 2004, *ApJ*, 607, 474  
 Honda, S., Aoki, W., Ishimaru, Y. et al. 2007, *ApJ*, 666, 1189  
 Hopkins, P. F. 2014, *ApJ*, 797, 59  
 Ito, H., Ozaki, Y., Suzuki, K. et al. 1988a, *JMoSp*, 127, 143  
 Ito, H., Ozaki, Y., Suzuki, K. et al. 1988b, *JMoSp*, 127, 283  
 Johnson, J. A. 2002, *ApJS*, 139, 219  
 Johnson, C. I., Rich, R. M., Kobayashi, C. et al. 2012, *ApJ*, 749, 175  
 Johnson, C. I., Rich, R. M., Kobayashi, C. et al. 2014, *AJ*, 148, 67  
 Kraft, R. P. 1994, *PASP*, 106, 553  
 Kruijssen, J. M. D. 2015, *MNRAS*, 454, 1658  
 Kotlar, A. J., Field, R. W., Steinfeld, J. I. et al. 1980, *JMoSp*, 80, 86  
 Kunder, A., Koch, A., Rich, R. M. et al. 2012, *AJ*, 143, 57  
 Larsson, M., Siegbahn, P. E. M., Agren, H. 1983, *ApJ*, 272, 369  
 Lawler, J. E., Bonvallet, G., Snenen, C. 2001a, *ApJ*, 556, 452  
 Lawler, J. E., Wickliffe, M. E., den Hartog, E. A. et al. 2001b, *ApJ*, 563, 1075  
 Lecureur, A., Hill, V., Zoccali, M. et al. 2007, *A&A*, 465, 799  
 Longmore, S. N., Kruijssen, J. M. D., Bastian, N., et al. 2014, *Protostars and Planets VI*, 291  
 Majewski, S. R., Schiavon, R. P., Frinchaboy, P. M. et al. 2015, arXiv:1509.05420  
 Marcassa, L. G., Muniz, S. R., Telles, G. D. et al. 1998, *OptCo*, 155, 38  
 Marcolini, A., Gibson, B. K., Karakas, A. I. et al. 2009, *MNRAS*, 395, 719  
 McWilliam, A., Wallerstein, G., Mottini, M. 2013, *ApJ*, 778, 149  
 Meléndez, J., Barbuy, B., Bica, E. et al. 2003, *A&A*, 411, 417  
 Meléndez, J., Barbuy, B. 2009, *A&A*, 497, 611  
 Mészáros, S., Martell, S. L., Shetrone, M. et al. 2015, *AJ*, 149, 153  
 Meynet, G., Ekström, S., Maeder, A. 2006, *A&A*, 447, 623  
 Modigliani, A., Mulas, G., Porceddu, I. et al. 2004, *Msngr*, 118, 8  
 Nakai, H., Jin, W.-G., Kawamura, M. et al. 2007, *JaJAP*, 46, 815  
 Ness, M., Asplund, M., Casey, A. R. 2014, *MNRAS*, 445, 2994  
 Niu, P., Cui, W., Zhang, B. 2015, *ApJ*, 813, 56  
 Noguchi, K., Aoki, W., Kawanomoto, S. et al. 2002, *PASJ*, 54, 855  
 Nomoto, K., Kobayashi, C., Tominaga, N. 2013, *ARA&A*, 51, 457  
 Pignatari, M., Gallino, R., Meynet, G. et al. 2008, *ApJ*, 687, L95  
 Piskunov, N. E., Kupka, F., Ryabchikova, T. A. et al. 1995, *A&AS*, 112, 525  
 Prasad, C. V. V. & Bernath, P. F. 1992, *JMoSp*, 156, 327  
 Prasad, C. V. V., Bernath, P. F., Frum, C. et al. 1992, *JMoSp*, 151, 459  
 Ramírez, I. & Allende Prieto, C. 2011, *ApJ*, 743, 135  
 Rehfuß, B. D., Suh, M.-H., Miller, T. A. et al. 1992, *JMoSp*, 151, 437  
 Renzini, A. 2008, *MNRAS*, 391, 354  
 Renzini, A., D'Antona, F., Cassisi, S. et al. 2015, *MNRAS*, 454, 4197  
 Rieke, G. H. & Lebofsky, M. J., 1985, *ApJ*, 288, 618  
 Roberts, L. F., Woosley, S. E. & Hoffman, R. D. 2010, *ApJ*, 722, 954  
 Roederer, I. U., Cowan, J. J., Karakas, A. I. et al. 2010, *ApJ*, 724, 975  
 Rutten, R. J. 1978, *Sol. Phys.*, 56, 237  
 Saito, R. K., Hempel, M., Minniti, D. et al. 2012, *A&A*, 537, A107  
 Schiavon et al. 2015, submitted  
 Schlafly, E. F. & Finkbeiner, D. P. 2011, *ApJ*, 737, 103  
 Schlegel, D. J., Finkbeiner, D. P., Davis, M. 1998, *ApJ*, 500, 525  
 Shapiro, K. L., Genzel, R., Förster Schreiber, N. M. 2010, *MNRAS*, 403, L36  
 Siqueira-Mello, C., Andrievsky, S. M., Barbuy, B. et al. 2015, *A&A*, 584, A86  
 Skrutskie, M. F., Cutri, R. M., Stiening, R. et al. 2006, *AJ*, 131, 1163  
 Snenen, C. A. 1973, *PhDT*, 180  
 Snenen, C., Cowan, J. J. & Gallino, R. 2008, *ARA&A*, 46, 241  
 Soto, M., Barbá, R., Gunthardt, G. et al. 2013, *A&A*, 552, A101  
 Travaglio, C., Gallino, R., Arnone, E. et al. 2004, *ApJ*, 601, 864  
 Tumlinson 2010, *ApJ* 708, 1398  
 Udalski, A., Szymanski, M., Kubiak, M. et al. 2002, *AcA*, 52, 217  
 Van der Swaelmen, M., Hill, V., Primas, F. et al. 2013, *A&A*, 560, A44  
 Van der Swaelmen, M., Barbuy, B., Hill, V. et al. 2016, *A&A*, 586, A1  
 Wahlin, R. & Plez, B. 2005, *ESASP*, 560, 1013  
 Wanajo, S., Ishimaru, Y. 2006, *Nucl. Phys. A*, 777, 676  
 Wanajo, S., Janka, H.-T. & Müller, B. 2011, *ApJ*, 726, L15  
 Wanajo, S. 2013, *ApJ*, 770, L22  
 Woosley, S. E. & Hoffman, R. D. 1992, *ApJ*, 395, 202  
 Woosley, S. E. & Weaver, Thomas A. 1995, *ApJS*, 101, 181  
 Yong, D., Alves-Brito, A., Da Costa, G. et al. 2014, *MNRAS*, 439, 2638  
 Zoccali, M., Lecureur, A., Barbuy, B. et al. 2006, *A&A*, 457, L1

## Appendix A: Line lists



**Table A.1.** Equivalent widths (EW) measured and used to derive new atmospheric parameters and iron abundances.

Species	$\lambda(\text{\AA})$	$\chi_{\text{ex}}(\text{eV})$	$\log g/\text{VALD}$	$\log g/\text{NIST}$	$\log g/\text{Adopted}$	Star 221		Star 224		Star 230		Star 235		Star 238	
						EW (mÅ)	A(Fe)	EW (mÅ)	A(Fe)	EW (mÅ)	A(Fe)	EW (mÅ)	A(Fe)	EW (mÅ)	A(Fe)
Fe I	6137.691	2.588	-1.403	-1.403	-1.403	—	—	113.5	6.62	73.4	5.80	159.3	6.86	156.9	6.97
Fe I	6151.618	2.176	-3.299	-3.299	-3.299	52.4	6.17	56.2	6.88	—	—	61.7	6.42	89.8	7.27
Fe I	6157.728	4.076	-1.260	-1.220	-1.220	70.8	6.93	48.4	6.77	52.5	6.80	57.6	6.62	70.2	7.08
Fe I	6159.377	4.608	-1.970	—	-1.970	—	—	—	—	8.0	6.85	—	—	—	—
Fe I	6165.360	4.143	-1.474	-1.474	-1.474	83.1	7.56	44.6	7.01	20.8	6.34	30.4	6.36	50.3	6.95
Fe I	6173.335	2.223	-2.880	-2.880	-2.880	78.2	6.39	46.2	6.27	32.8	5.86	90.3	6.69	—	—
Fe I	6180.204	2.727	-2.586	-2.649	-2.649	73.3	6.70	36.6	6.40	19.9	5.87	—	—	79.3	7.07
Fe I	6187.990	3.943	-1.720	-1.670	-1.670	49.9	6.71	22.0	6.42	—	—	42.7	6.58	57.2	7.05
Fe I	6200.313	2.608	-2.437	-2.437	-2.437	47.6	5.75	—	—	64.3	6.63	69.8	6.28	—	—
Fe I	6213.430	2.223	-2.482	-2.482	-2.482	102.9	6.54	94.6	6.97	82.0	6.64	105.8	6.61	121.8	7.11
Fe I	6219.281	2.198	-2.433	-2.433	-2.433	—	—	92.5	6.85	88.9	6.71	114.3	6.70	141.8	7.32
Fe I	6220.783	3.882	-2.460	—	-2.460	9.8	6.33	—	—	—	—	11.8	6.47	26.2	7.07
Fe I	6226.736	3.882	-2.220	—	-2.220	49.3	7.17	—	—	—	—	15.3	6.37	—	—
Fe I	6229.228	2.845	-2.805	-2.805	-2.805	56.0	6.60	64.5	7.35	42.1	6.72	50.7	6.53	50.8	6.72
Fe I	6240.646	2.223	-3.233	-3.173	-3.173	36.7	5.77	52.0	6.71	41.5	6.36	58.0	6.28	80.2	7.01
Fe I	6246.318	3.602	-0.733	-0.877	-0.877	102.5	6.65	98.2	6.80	66.4	6.18	92.5	6.43	—	—
Fe I	6252.555	2.404	-1.687	-1.687	-1.687	133.1	6.59	113.5	6.70	78.8	5.99	133.4	6.58	150.3	6.97
Fe I	6254.258	2.279	-2.443	-2.426	-2.426	114.0	6.92	68.7	6.43	103.7	7.13	146.7	7.49	129.3	7.38
Fe I	6265.133	2.176	-2.550	-2.550	-2.550	101.8	6.52	76.5	6.60	49.0	5.85	104.7	6.59	115.6	7.02
Fe I	6270.225	2.858	-2.464	-2.609	-2.609	46.6	6.21	40.4	6.59	—	—	61.0	6.56	72.7	7.03
Fe I	6271.278	3.332	-2.703	-2.703	-2.703	25.8	6.43	—	—	32.9	6.95	21.3	6.37	49.1	7.16
Fe I	6297.793	2.223	-2.740	-2.740	-2.740	100.5	6.74	68.0	6.64	71.8	6.65	—	—	122.7	7.38
Fe I	6301.501	3.654	-0.718	-0.718	-0.718	77.5	6.02	—	—	—	—	97.1	6.41	103.8	6.68
Fe I	6302.493	3.686	-0.973	—	-0.973	—	—	—	—	61.6	6.26	87.5	6.51	—	—
Fe I	6311.500	2.832	-3.141	-3.141	-3.141	61.2	7.03	—	—	—	—	35.0	6.52	53.8	7.10
Fe I	6315.306	4.143	-1.232	-1.232	-1.232	60.7	6.77	70.1	7.34	39.3	6.57	65.3	6.88	77.9	7.33
Fe I	6315.811	4.076	-1.710	-1.660	-1.660	43.7	6.72	45.5	7.14	37.2	6.87	37.4	6.61	39.5	6.81
Fe I	6322.685	2.588	-2.426	-2.426	-2.426	86.4	6.60	84.1	7.11	—	—	92.4	6.75	104.1	7.20
Fe I	6335.330	2.198	-2.177	-2.177	-2.177	94.6	6.01	88.6	6.50	79.6	6.24	119.0	6.50	130.8	6.89
Fe I	6336.824	3.686	-0.856	-0.856	-0.856	80.6	6.26	74.5	6.47	64.8	6.21	88.8	6.42	95.2	6.70
Fe I	6344.149	2.433	-2.923	-2.923	-2.923	77.5	6.68	—	—	48.7	6.51	82.2	6.82	104.9	7.53
Fe I	6355.029	2.845	-2.350	-2.291	-2.291	83.6	6.72	78.8	7.15	75.8	7.01	86.5	6.79	106.6	7.41
Fe I	6380.743	4.186	-1.376	-1.376	-1.376	56.5	6.86	30.9	6.63	32.9	6.61	37.7	6.46	61.7	7.15
Fe I	6392.538	2.279	-4.030	—	-4.030	42.9	6.81	45.0	7.44	—	—	30.9	6.63	39.7	7.00
Fe I	6393.601	2.433	-1.432	-1.576	-1.576	112.8	6.12	88.3	6.17	87.0	6.07	143.0	6.61	161.6	6.98
Fe I	6408.018	3.686	-1.018	-1.018	-1.018	69.1	6.17	77.1	6.77	67.2	6.49	83.8	6.51	93.1	6.89
Fe I	6411.649	3.653	-0.595	-0.718	-0.718	95.5	6.39	96.6	6.66	69.8	6.14	98.6	6.43	104.3	6.67
Fe I	6419.949	4.733	-0.240	-0.270	-0.270	77.6	6.88	—	—	75.1	7.00	57.8	6.44	—	—
Fe I	6421.350	2.279	-2.027	-2.027	-2.027	148.3	7.13	141.5	7.28	92.7	6.50	130.6	6.79	136.6	7.06
Fe I	6430.846	2.176	-2.006	-2.006	-2.006	108.4	6.08	121.0	6.83	77.3	5.98	138.4	6.59	149.3	6.92
Fe I	6469.193	4.835	-0.770	-0.810	-0.810	71.2	7.40	—	—	—	—	—	—	56.7	7.21
Fe I	6475.624	2.559	-2.942	-2.942	-2.942	74.4	6.78	59.7	7.02	62.4	7.01	73.2	6.78	84.4	7.25
Fe I	6481.870	2.279	-2.984	-2.984	-2.984	87.5	6.74	73.5	7.05	54.1	6.51	74.6	6.48	93.4	7.11
Fe I	6494.980	2.404	-1.273	-1.273	-1.273	149.0	6.35	123.8	6.40	123.4	6.33	—	—	165.9	6.68
Fe I	6498.939	0.958	-4.699	-4.687	-4.687	119.9	7.55	80.1	7.40	—	—	86.5	6.77	101.1	7.38
Fe I	6518.367	2.832	-2.460	-2.298	-2.298	66.5	6.29	55.8	6.59	45.6	6.27	73.6	6.47	73.2	6.67
Fe I	6533.929	4.558	-1.430	-1.430	-1.430	—	—	—	—	—	—	22.4	6.59	—	—
Fe I	6546.239	2.759	-1.536	-1.536	-1.536	114.7	6.51	85.7	6.43	79.0	6.22	114.3	6.49	137.9	7.04
Fe I	6569.215	4.733	-0.420	-0.450	-0.450	54.7	6.54	59.9	6.93	38.1	6.40	54.2	6.54	80.7	7.23
Fe I	6574.228	0.990	-5.023	-5.004	-5.004	59.0	6.44	68.1	7.45	57.8	7.10	—	—	81.6	7.26
Fe I	6575.015	4.733	-2.710	-2.710	-2.710	83.4	6.78	67.0	6.99	58.1	6.69	76.0	6.63	92.4	7.21
Fe I	6581.210	1.485	-4.679	-4.679	-4.679	53.9	6.66	43.7	7.13	—	—	—	—	—	—
Fe I	6593.870	2.433	-2.422	-2.422	-2.422	—	—	—	—	77.8	6.70	103.1	6.74	—	—
Fe I	6597.561	4.795	-1.070	-1.050	-1.050	76.0	7.69	55.8	7.50	17.7	6.54	24.0	6.54	—	—
Fe I	6608.026	2.279	-4.030	—	-4.030	62.6	7.21	46.0	7.45	—	—	40.6	6.81	47.4	7.15
Fe I	6609.110	2.559	-2.692	-2.692	-2.692	85.6	6.77	81.6	7.26	27.7	5.91	81.6	6.70	101.6	7.35
Fe I	6627.544	4.548	-1.680	—	-1.680	24.0	6.84	—	—	—	—	—	—	27.8	7.10
Fe I	6677.986	2.692	-1.418	-1.418	-1.418	128.8	6.53	—	—	95.2	6.35	139.8	6.68	138.6	6.84
Fe I	6699.141	4.593	-2.101	-2.101	-2.101	—	—	—	—	—	—	—	—	7.3	6.83
Fe I	6703.567	2.759	-3.160	-3.060	-3.060	81.6	7.29	56.7	7.28	—	—	46.5	6.56	68.6	7.23
Fe I	6705.102	4.607	-1.392	—	-1.392	54.7	7.32	39.2	7.28	—	—	30.9	6.82	45.4	7.27
Fe I	6710.319	1.485	-4.880	—	-4.880	54.2	6.86	45.8	7.37	—	—	32.4	6.49	57.6	7.22
Fe I	6713.744	4.795	-1.600	—	-1.600	—	—	—	—	—	—	10.3	6.61	23.2	7.19
Fe I	6715.383	4.608	-1.640	—	-1.640	—	—	—	—	17.0	6.89	12.0	6.51	35.0	7.30
Fe I	6725.357	4.103	-2.300	—	-2.300	—	—	14.3	6.96	16.4	6.96	17.7	6.77	21.4	7.02
Fe I	6726.666	4.607	-1.133	—	-1.133	—	—	52.7	7.31	31.8	6.78	31.5	6.57	46.7	7.04
Fe I	6733.151	4.638	-1.580	—	-1.580	—	—	16.0	6.90	—	—	17.4	6.68	—	—
Fe I	6739.521	1.557	-4.794	-4.794	-4.794	47.0	6.71	23.8	6.85	—	—	34.8	6.55	38.0	6.82
Fe I	6752.707	4.638	-1.204	-1.204	-1.204	24.7	6.48	—	—	—	—	11.6	6.09	—	—
Fe II	6084.103	3.199	-3.780	-3.900	-3.790*	—	—	—	—	—	—	19.0	6.66	25.7	7.33
Fe II	6149.246	3.890	-2.720	-2.800	-2.690*	—	—	—	—	11.2	6.18	22.9	6.48	18.4	6.74
Fe II	6247.559	3.892	-2.310	-2.400	-2.300*	—	—	45.3	7.20	31.9	6.51	37.6	6.51	38.3	6.99
Fe II	6416.930	3.892	-2.650	-2.900	-2.640*	—	—	—	—	—	—	27.7	6.58	28.3	7.04
Fe II	6432.677	2.891	-3.520	-3.500	-3.570*	42.2	6.71	35.3	7.10	33.0	6.69	33.6	6.51	38.5	7.12
Fe II	6456.380	3.903	-2.100	-2.200	-2.050*	26.5	5.95	32.7	6.62	38.5	6.45	43.7	6.43	50.4	7.08
Fe II	6516.077	2.891	-3.320	-3.370	-3.310*	43.2	6.47	29.0	6.67	35.2	6.49	51.0	6.67	50.9	7.17

References. \*: Meléndez &amp; Barbuy (2009).

**Table A.2.** List of lines used in the present analysis, with the individual abundances.

Species	$\lambda(\text{\AA})$	$\chi_{ex}(\text{eV})$	$\log gf$	A(X) 221	A(X) 224	A(X) 230	A(X) 235	A(X) 238
[O I]	6300.311	0.000	-9.716	+8.40	—	+8.25	+8.40	+8.85
Na I	4982.813	2.104	-0.962	—	+5.45	—	—	—
Na I	5688.205	2.104	-0.450	—	—	+4.70	+5.22	+5.88
Na I	6154.230	2.102	-1.560	+5.65	—	—	+5.18	—
Na I	6160.753	2.104	-1.260	+5.70	+5.70	+5.10	+5.22	+5.98
Mg I	5528.405	4.346	-0.498	—	—	—	+6.90	—
Mg I	6318.720	5.108	-2.100	+7.22	+7.50	+7.18	+7.18	+7.35
Mg I	6319.242	5.110	-2.360	—	+7.50	—	+7.30	—
Mg I	6765.450	5.750	-1.940	—	—	+7.20	—	+7.55
Al I	6696.015	3.143	-1.569	+6.00	+6.30	+5.64	+5.85	+6.25
Al I	6698.673	3.143	-1.870	+6.00	+6.28	+5.90	+5.72	+6.21
Si I	5665.555	4.920	-2.040	—	—	+6.90	—	—
Si I	5690.425	4.930	-1.870	+6.70	—	—	+6.85	+7.18
Si I	5948.545	5.082	-1.300	—	+7.14	—	+6.75	+7.25
Si I	6142.494	5.619	-1.500	—	+7.32	+6.80	+6.77	+7.40
Si I	6145.020	5.616	-1.450	+7.00	—	+6.95	+6.77	+7.15
Si I	6155.142	5.619	-0.850	+6.96	+7.35	+6.90	+6.76	—
Si I	6237.328	5.614	-1.010	—	+7.25	—	—	—
Si I	6243.823	5.616	-1.300	—	+7.20	+7.00	—	+7.15
Si I	6414.987	5.870	-1.130	+6.80	—	+7.30	—	—
Si I	6721.844	5.860	-1.170	—	—	—	+6.80	—
Ca I	5601.277	2.526	-0.520	—	—	—	+5.70	+6.00
Ca I	5867.562	2.933	-1.550	—	+6.20	—	+5.72	+6.00
Ca I	6102.723	1.879	-0.793	+5.75	+6.00	+5.40	+5.70	+6.22
Ca I	6122.217	1.886	-0.200	—	—	—	+5.85	+5.85
Ca I	6156.030	2.521	-2.390	+6.00	—	—	+5.55	+6.10
Ca I	6161.295	2.510	-1.020	—	+5.90	+5.35	—	+6.00
Ca I	6162.167	1.899	-0.090	+5.50	+5.80	+5.40	+5.70	+6.00
Ca I	6166.440	2.521	-0.900	—	—	+5.40	—	—
Ca I	6169.044	2.523	-0.540	+5.50	+5.85	+5.40	—	+5.95
Ca I	6169.564	2.526	-0.270	+5.50	+5.80	+5.42	—	+5.80
Ca I	6439.080	2.526	+0.300	+5.75	+5.90	+5.50	+5.85	+6.15
Ca I	6455.605	2.523	-1.350	+5.45	+5.90	+5.70	+5.80	+6.25
Ca I	6462.567	2.523	+0.262	—	—	—	—	+5.90
Ca I	6464.679	2.523	-2.100	+5.60	—	—	+5.50	+6.00
Ca I	6471.668	2.526	-0.590	—	+6.00	+5.42	+5.90	+6.30
Ca I	6493.788	2.521	+0.000	+5.70	+6.10	—	+5.83	—
Ca I	6499.654	2.523	-0.850	+5.60	+5.90	—	+5.90	+6.28
Ca I	6572.779	0.000	-4.320	+5.80	+6.35	—	+5.80	+6.38
Ca I	6717.687	2.709	-0.610	+5.90	+6.45	+5.65	+5.70	+6.48
Ti I	5689.459	2.230	-0.400	—	+4.65	—	+4.32	+4.55
Ti I	5866.449	1.067	-0.840	—	+4.70	+4.00	+4.45	—
Ti I	5922.108	1.046	-1.460	+4.38	+4.94	+4.50	+4.45	+5.00
Ti I	5941.750	1.053	-1.530	—	+4.50	+4.50	+4.40	—
Ti I	5965.825	1.879	-0.420	+4.32	+4.45	+4.10	+4.32	+4.85
Ti I	5978.539	1.873	-0.530	+4.45	+4.75	—	+4.36	—
Ti I	6126.224	1.070	-1.430	+4.35	+4.45	+4.40	+4.45	+4.82
Ti I	6258.110	1.440	-0.360	+4.25	+4.55	+4.25	+4.20	+5.00
Ti I	6261.106	1.430	-0.480	+4.20	+5.00	+4.20	+4.40	+5.00
Ti I	6336.113	1.440	-1.740	+4.60	+4.80	—	+4.35	+4.85
Ti I	6554.238	1.440	-1.220	+4.42	+4.80	+4.30	+4.38	+4.85
Ti I	6556.077	1.460	-1.070	+4.35	—	—	+4.46	—
Ti I	6599.113	0.900	-2.090	+4.50	+4.96	—	+4.50	+4.90
Ti I	6743.127	0.900	-1.730	—	—	—	+4.45	+4.87
Ti II	5336.771	1.582	-1.700	—	—	—	+4.40	+4.75
Ti II	5381.021	1.566	-2.080	—	—	—	+4.40	—
Ti II	5418.751	1.582	-2.130	—	—	—	+4.30	—
Ti II	6491.580	2.060	-2.100	+4.42	+4.95	+4.35	+4.43	+4.88
Ti II	6559.576	2.050	-2.350	+4.60	+4.75	+4.46	—	+4.95
Ti II	6606.970	2.060	-2.850	—	+4.70	+4.20	—	+4.70
Y I	6435.004	0.066	-0.820	+1.60	+1.95	+1.90	+1.60	+1.92
Zr I	6127.475	0.154	-1.050	+2.50	—	+2.40	+2.38	—
Zr I	6134.585	0.000	-1.280	—	—	—	+2.40	+2.55
Zr I	6143.252	0.071	-1.100	—	+2.60	—	+2.20	+2.65
Ba II	6141.713	0.704	+0.000	+1.50	+1.80	+1.25	+1.80	+2.00
Ba II	6496.897	0.604	-0.320	+1.70	—	+2.00	+2.00	+2.20
La II	6320.376	0.170	-1.560	+0.30	+0.85	—	+0.45	+0.90
La II	6390.477	0.321	-1.410	—	+1.20	—	+0.70	+0.80
La II	6774.268	0.126	-1.708	—	—	—	+0.90	—
Eu II	6437.640	1.320	-0.320	+0.00	+0.35	+0.00	+0.00	+0.56
Eu II	6645.064	1.380	+0.120	—	—	-0.20	+0.10	—